universität wien

# MASTERARBEIT / MASTER'S THESIS

Titel der Masterarbeit / Title of the Master's Thesis

## An Analysis of the Complex Organic Molecules of the Hot Corino around low-mass Protostar SMM1a


verfasst von / submitted by

Sophie Alma Schallert BSc


angestrebter akademischer Grad / in partial fulfilment of the requirements for the degree of

Master of Science (MSc)

Wien, 2020 / Vienna, 2020

| | |
|---|---|
| Studienkennzahl lt. Studienblatt / degree programme code as it appears on the student record sheet: | A 066 861 |
| Studienrichtung lt. Studienblatt / degree programme as it appears on the student record sheet: | Masterstudium Astronomie |
| Betreut von / Supervisor: | Uni.-Prof. Dr. Manuel Güdel |
| Mitbetreut von / Co-Supervisor: | MMag. Odysseas Dionatos PhD |

# Abstract

*Context.* In this thesis the complex organic molecules (COMs) of the protostellar binary SMM1 in the Serpens main star formation region are analysed. The excitation conditions (the excitation temperature and the column density) of the identified species towards SMM1a and SMM1b are analysed and put into context with similar sources, namely other hot corinos.

*Aims.* This thesis aims to determine the abundances of COMs towards the protostellar binary SMM1a and to compare them to other hot corinos.

*Methods.* The used observational ALMA Band 6 data towards SMM1 was taken in 2015 and 2018 in the course of two different surveys. The species were identified by comparing the fitted extracted spectra to the synthetic spectra as well as the probable species for each transition. The excitation temperature and column density of a species were calculated under the assumptions of local thermodynamic equilibrium and that all transitions are optically thin and thermalized. The abundance ratios are taken with respect to $CH_3OH$ and the deuteration fraction of formaldehyde was taken with respect to its doubly deuterated isotopologue $D_2CO$.

*Results.* The excitation temperature and column density for 10 different species could be calculated towards SMM1a and for 5 species towards SMM1b. The excitation temperatures and column densities of the species are comparable to those of other hot corinos like HH 212, IRAS 16293-2422 A and B. $CH_3OH$ is an exception, where the column density is 1-3 orders of magnitude lower as compared to other sources. This influences the abundance ratio of the different species and leads to a generally higher abundance as compared to other hot corinos. The species could be divided into two groups, one tracing the hot (> 100 K) gas component near the central protostar and one tracing the more extended colder (< 100 K) regions of the hot corino, except for $CH_3OCHO$ where the excitation temperature is too low compared to the binding energy. The two protostellar binary sources SMM1a and SMM1b show a difference in number and intensity of the transitions, with SMM1b having only a fourth of the number of transi-

tions of SMM1a. The D/H ratio of SMM1a is comparable to the formaldehyde deuteration of IRAS 16293-2422.
*Conclusions.* The abundances in relation to $CH_3OH$ of the 10 identified species as well as the D/H ratio are comparable to those of other hot corinos. These hot corinos are located in different star forming regions with different properties, which could indicate that for these sources a similar formation scheme could be applied. The difference in the number of transitions between SMM1a and SMM1b might point to SMM1b being in a different evolutionary stage, but which scenario applies for this source is not clear.

# Abstract german

*Kontext.* Diese Masterarbeit konzentriert sich auf die Analyse der COMs (complex organic molecules) des protostellaren Binärsystems SMM1 im Sternenstehungsgebiet Serpens. Die Anregungstemperatur und die Säulendichte der identifizierten molekularen Spezies von SMM1a und SMM1b werden berechnet und mit anderen Hot Corinos verglichen.

*Ziel.* Das Ziel dieser Masterarbeit ist es, die relativen Häufigkeiten der COMs des protostellaren Binärsystems SMM1a in den Kontext zu anderen Hot Corinos zu stellen.

*Methoden.* Die analysierten Daten wurden 2015 und 2018 mit dem ALMA Teleskop aufgenommen. Die Identifizierung der verschiedenen Spezies erfolgte über den Vergleich der extrahierten Spektren zu den berechneten Spektren und den erwarteten Spezies für die Spektrallinien. Die Anregungstemperatur und die Säulendichte der Spezies wurden unter den Annahmen von lokalem thermodynamischen Gleichgewicht und optisch dünnen und thermalisierten Übergängen berrechnet. Die Häufigkeiten sind in Relation zu $CH_3OH$ und die Fraktionierung von Formaldehyd in Relation zu $D_2CO$ angegeben.

*Ergebnisse.* Für 10 Spezies in SMM1a und für 5 Spezies in SMM1b konnten die Anregungstemperatur und die Säulendichte berechnet werden. Diese sind vergleichbar zu anderen Hot Corinos, außer für die Säulendichte von $CH_3OH$, bei dieser Spezies ist diese um 1-3 Größenordnungen kleiner im Vergleich zu anderen ähnlichen Objekten. Das nimmt Einfluss auf die Häufigkeiten, welche für SMM1a und SMM1b generell höher sind im Vergleich zu anderen Hot Corinos wie HH 212 und IRAS 16293-2422. Die identifizierten Spezies konnten über die Anregungstemperatur in zwei Gruppen geteilt werden, eine für das heiße (> 100 K) Gas in der kompakten inneren Gegend und eine für die weiter ausgedehnte kältere (<100 K) Komponente. Diese Einteilung war nicht möglich für $CH_3OCHO$, da die Temperatur zu niedrig war im Vergleich zu der hohen Bindungsenergie. Die Anzahl von Spektrallinien ist geringer in SMM1b im Vergleich zu SMM1a. Das D/H Verhältnis von SMM1a ist vergleichbar zu dem von

IRAS 16293-2422.

*Fazit.* Die Häufigkeiten in Relation zu $CH_3OH$ der identifizierten Spezies von SMM1a und SMM1b sind verleichbar zu denen von anderen Hot Corinos, was zu dem Schluss führen kann, dass für diese Objekte eine ähnliches Enstehungsschema angewendet werden kann, da sie sich in verschiedenen Umgebungen mit verschiedenen physikalischen Eigenschaften befinden. Der Unterschied in der Anzahl der Spekrallinien könnte ein Indiz dafür sein, dass dieses Objekt sich in einer anderen Phase der Entwicklung befindet als SMM1a.

# Contents

# Chapter 1

# Introduction

Complex organic molecules (COMs) are molecules which have at least 6 atoms with at least one of them being a carbon atom (Herbst & van Dishoeck, 2009). They are important as they carry a substantial fraction of carbon that can be used for prebiotic chemistry (De Simone et al., 2020) and have a potential role in the formation of terrestrial life (Vastel et al., 2014). They are found in many different astrophysical environments, hot cores and hot corinos, toward prestellar cores, cold envelopes, the Galactic Center, cold clouds, outflow driven shocks and various solar system objects, such as comets (Jørgensen et al., 2020). This thesis concentrates on the COMs in Class 0 hot corinos, where complex organic molecules are liberated into the gas phase for the first time after they have formed on dust grains.

A hot corino is a hot (>100 K), compact (< 100 au) and dense (> $10^6$ cm$^{-3}$) environment enriched by a large number of COMs. This region is a part of the sources protostellar envelope and surrounds a central young stellar object (YSO), which in this case is the Class 0 low mass protostar SMM1a. The Class 0 YSO has no clear disk and is deeply embedded in its protostellar envelope, which makes submillimeter/millimeter observations necessary to study these objects. In this phase about 50% of the star's final mass is accreted in a short period of time (~$10^4$ years).

Hot corinos are still rarely detected, but in the last few years starting with the first detection in 2003 by Cazaux et al. (2003), the number of identified hot corinos has increased to about 13 Class 0/Class I hot sources. Studying this early evolutionary stage of star formation could be important in the context of planet formation as it is thought that this formation process starts as early as the Class 0/Class I stage (Gelder et al., 2020).

The outline of the thesis is an introduction into the topic with more detailed explanations of protostars, COMs, hot corinos and other important processes, like fractionation. An introduction into the analysed source is given in section 1.4 and the underlying observational concepts are described in section 1.6. The second Chapter concentrates on the used methods and tools for the data analysis. Chapter 3 presents the results of the data analysis, which are discussed in Chapter 4.

## 1.1 Protostars

### 1.1.1 Molecular cloud collapse

The star formation process begins with a molecular cloud, which becomes gravitationally instable. To describe this instability which leads to the cloud collapse a general look at the properties of the molecular cloud and the working forces is needed. The Virial theorem gives the equilibrium of all energy terms and their interaction with each other for stability. It is derived from the Magentohydrodynamic (MHD) equations of motion, which are used to describe the properties of the gas. The different forces in this equilibrium are self gravity and the external pressure working towards a collapse and the thermal pressure and the magnetic field working against a collapse.
The Jeans instability describes the interaction of pressure against self gravity in an uniform infinite medium, without heating processes (isothermal) and no magnetic field. This approximated equilibrium gets disturbed in density, pressure and gravitational potential. These perturbations get incorporated into the hydrodynamic equations of motion and by solving them, we get a criterion on the instability of such a cloud. This instability criterion is given by the Jeans length:

$$\lambda > \lambda_J = \left(\frac{\pi}{G \cdot \rho_0}\right)^{1/2} \cdot c_s \tag{1.1}$$

A constraining factor for the mass is given by the Jeans mass:

$$M_J \propto \left(\frac{T^3}{\rho}\right)^{1/2} \tag{1.2}$$

The different parameters are the diameter of the sphere/cloud $\lambda$, the gravitational constant $G$, the density of the gas $\rho$, the thermal sound speed in the core $c_s = \sqrt{\frac{kT}{m}}$ and the temperature $T$. The critical mass can also be described by a Bonnor-Ebert-Sphere, which gives a more exact criterion for the maximum mass

of a spherical cloud that can support itself against a collapse by thermal pressure, as it includes the external pressure $P_{ext}$:

$$M_{crit} = 3.55 \cdot \frac{c_s^4}{G^{3/2} \cdot P_{ext}^{1/2}} \tag{1.3}$$

These criteria use the thermal pressure as an opposing factor against the gravitational collapse of a sphere, but as mentioned above a magnetic field can also stabilize a molecular cloud. To describe this we assume that the magnetic field is uniformly distributed within the sphere and the magnetic flux $\Phi$ does not change as a cloud expands or contracts due to flux-freezing (Krumholz, 2015). From the Virial theorem we get a critical mass of:

$$M_{crit} \approx \frac{0.12}{G^{1/2}} \cdot \Phi \tag{1.4}$$

The critical mass criteria with or without a magnetic field do not work for all molecular clouds and are of course simplifications of reality, as molecular clouds are not spherical and have no uniform distribution of magnetic field or density. But nonetheless these criteria can be used to describe collapses. The Jeans criterion for a collapse is too efficient and as such only works for smaller molecular clouds. The instability considering the magnetic field is too inefficient in its collapse, as the magnetic field is a strong support against a gravitational collapse. It only works in describing bigger molecular cloud collapses. (Mouschovias, 1976) During the contraction the temperature of a cloud increases and in turn the density also increases as $T \sim \rho^{2/3}$, which in turn would increase the Jeans mass as seen in the relation 1.2. At some point the Jeans mass would reach the cloud mass, which would lead again to a Virial equilibrium and contraction would stop. This scenario is not occurring due to the cooling of the cloud through radiative losses. The cooling is effective when emitting in the IR, as the clouds are optically thick. The main cooling agents in molecular clouds are: emission by molecules and emission by dust. These cooling mechanisms result in the cloud to form contracting substructures, which leads to fragmentation. When these fragments reach hydrostatic equilibrium they are called clumps. On this clump the surrounding gas keeps falling, which forms the pre-stellar dense core. The formation of this core takes about 1 Myr. Then the central protostar is formed. (Lamers & Levesque, 2017)

### 1.1.2 Protostar evolution

The classification of young stellar objects (YSO) was initially conducted through the shapes of their spectral energy distributions (SED), which primariliy tracks the evolution of the circumstellar components. In 1987 Lada identified three distinct classes I, II and III. André et al. (1993) added the Class 0 YSO to the evolutionary path of protostars as they found a YSO so deeply embedded that it radiates large amounts of far-infrared and sub-millimeter emission relative to total luminosity, which would not fit in the existing classification. They also proposed an additional criterion in the classification of YSOs, the ratio of the submillimeter to the bolometric luminosity. In the same year another criterion was proposed by Myers & Ladd (1993), the bolometric temperature. These classifications with an illustration of the different classes is shown in figure 1.1.
The first object described in the protostellar phase is the Class 0 YSO. This young protostar has no clear disk and is embedded in its protostellar envelope, which makes submillimeter/millimeter observations necessary to study this object,
which is possible with instruments such as ALMA. The SED resembles a cold black body with temperatures of about 15-30 K, which indicates that the circumstellar envelope is the dominant component with $M_* \ll M_{env}$ (André, 2011). This object is in its main accretion phase, where 50% of the final stars mass is accreted during a quite short period of time, namely during about $10^4$ years. The accreation rate is about $10^{-6}$ - $10^{-5}$ $M_\odot$/year. They are further characterized by high ratios of submillimeter to bolometric luminosity $L_{submm}/L_{bol} > 1\%$ (André, 2011). Another characteristic of Class 0 sources is that they are associated with powerful highly collimated bipolar outflows, which are broader in Class I sources. The next evolutionary stage is the Class I YSO, the evolved accreting protostar, which lasts for ~$10^5$ years. The accretion rate already drops to $10^{-7}$ - $10^{-6}$ $M_\odot$/year and a clear disk surrounding the protostar can be detected, but a circumstellar envelope is still present although only as a remnant ($M_* > M_{env}$). The SEDs here show a rise towards longer wavelengths, indicating an excess of far-infrared emission. Part of the increased luminosity comes from the accretion of the circumstellar material. After the protostellar phase the pre-main sequence phase follows with the Class II and III objects. Class II objects are also called classical T Tauri stars and are surrounded by an optically thick cirumstellar disk with a mass of ~0.01 $M_\odot$. This disk further evolves to an optically thin debris disk in the weak T Tauri star (Class III) stage with $M_{disk} < M_{Jupiter}$. The mass accretion rate also drops during the further evolution of a T Tauri star from $10^{-7}$ $M_\odot$/year (Class II) to $10^{-9}$ $M_\odot$/year or lower (Class III) (André, 2011). After another $10^7$ years the star en-

ters the main sequence and the disk may have formed planets and other objects.

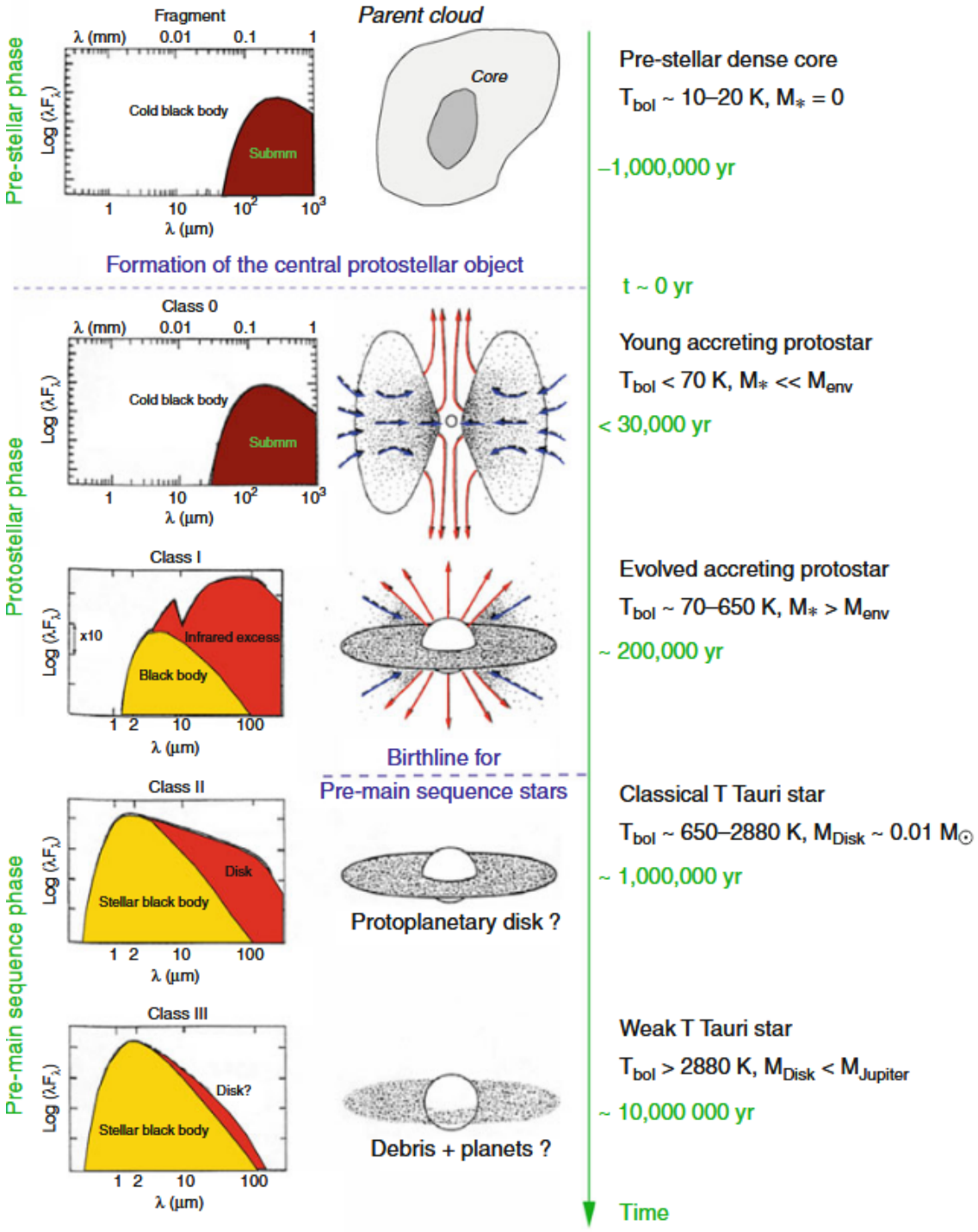


Figure 1.1: Showing the different stages of the star formation process.
Image credit: André (2011)

## 1.2 Complex Organic Molecules

### 1.2.1 Where are they found?

COMs are found in hot environments such as hot corinos or hot cores, but they are also found toward prestellar cores, cold envelopes, the Galactic Center, cold clouds, outflow driven shocks and various solar system objects, such as comets. COMs are detected in the gas phase, in which they are liberated through continuous thermal evaporation of the ices they are frozen into. This process is called thermal desorption, with dust temperatures reaching ~85 K, and is the main desorption process. There are also other processes which occur in colder environments, such as cold prestellar cores or cold envelopes, where thermal desorption does not play a role. These additional non-thermal effects are photodissociation, reactive desorption, and energetic interaction. Sahu et al. (2019) argues that these processes may enhance the gas phase abundances of chemical species like COMs, but through processes like photodissociation molecules get destroyed and leave fewer COM in some areas.
The detection of COMs towards outflow driven shocks reveals for instance for the brightest shock region of the protostar L1157 a clear chemical segregation. In different areas of the shock Acetaldehyde and Formamide are found and seem to indicate a chemical evolutionary effect within the shock region (Codella et al., 2017).
In our solar system objects like comets harbour different complex molecules. Previous space missions like the NASA Starburst mission found that some cometary grains contain glycine, which is the simplest amino acid[1] (Elsila et al., 2009). An interesting comet is 67/Churyumov-Gerasimenko, where the COSAC instrument on the ROSETTA mission found several organic compounds. Part of these compounds were numerous carbon- and nitrogen rich molecules in the cometary ices (Gudipati et al., 2015). This chemical composition of comets and also planetesimals could be partially inherited from the pre- and protostellar phases of the evolution of a low mass star according to Drozdovskaya et al. (2019).

### 1.2.2 Formation

Complex organic molecules are often classified as such when they have at least 6 heavy atoms and are of importance due to their potential role in the formation of terrestrial life (Vastel et al., 2014). Furthermore they could help in understanding

[1] Amino acids are residues in proteins and are important for tissues and muscles of humans as they cannot be produced by them. Due to that they are ubiquitous in biochemistry.

the chemical evolution of matter during the formation of stars and planets.
The dominating formation process of COMs is thermal and UV processing of earlier formed organic molecules in icy mantels of grains or on their surface. Reactive radicals are a result of cosmic ray induced UV photons colliding with gas-phase particles, which then photodissociate molecules in the ices (Jørgensen et al., 2020).
For instance Methanol ($CH_3OH$), which is formed on the surface ices through repeated hydrogenation of CO (Sahu et al., 2019) produces radicals in the ices and is especially important in the formation of complex molecular structures. A warm environment (20-100K) allows radicals like $CH_3$ and $CH_2OH$ to diffuse and then recombine to form complex molecules. This process then reoccurs until all the ice is evaporated and released into the gas phase. Other formation routes for example for smaller species include atomic accretion and recombination on grain surfaces, hydrogenation of molecules and radicals or a combination of hydrogenation and oxidation (Öberg et al., 2009).

## 1.3 Hot Corinos

Hot corinos are the analog of a hot core, but for low mass protostars. A hot core as a product of high mass star formation is characterized physically by a high tempererature of both gas and dust (> 100 K) and high gas densities exceeding $10^6$ cm$^{-3}$ (Cazaux et al., 2003). Additionally the gas contains many complex organic molecules, which are as mentioned in section 1.2 evaporated from the ice mantels of dust grains. This hot environment is produced by the luminosity of the protostar and the protostellar accretion disk. Another contributing factor in the chemical composition and temperature may be shock waves (Ceccarelli et al., 2006).
The first hot core belonging to a low mass protostar was discovered in 2003 by Cazaux et al. (2003), where they found that IRAS 16293-2422 showed signatures of a hot core. The source had an elevated temperature and gas density near the protostar. The gas was enriched in molecules and showed a high level of deuteration, which is higher than in the one found in high mass hot cores. They also argued that low mass hot cores are smaller and colder than massive hot cores. The chemical composition also seemed to be different between these two classes of protostars.
The term hot corino itself was established in 2004 by Ceccarelli to make a clear distinction between the hot and chemically enriched environment around a pro-

tostar of low mass in contrast to the hot core associated with a high mass protostar. The second source observed and analysed in this context was NGC 1333 IRAS 4A by Bottinelli et al. (2004) in the same year. In the following years other hot corinos were identified, such as NGC 1333 IRAS 4B and IRAS 2A by Bottinelli et al. (2007). Both IRAS 16293-2422 and NGC 1333 IRAS 4A later on revealed themselves to be binary systems. The NGC 1333 IRAS 4A binary harbours the hot corino A2 and the source A1 shows hot corino like features, but is still to be clearly identified as one (Sahu et al., 2019). IRAS 16293-2422 A was well studied during the ALMA-PILS survey by Jørgensen et al. (2016), Jørgensen et al. (2018), Manigand et al. (2019), Manigand et al. (2020) and Lykke et al. (2017), where further COMs and isotopologues were detected and analysed. In the following years other Class 0 protostar hot corinos were found such as NGC 1333 IRAS 2A (Jørgensen et al., 2005) and NGC 1333 IRAS 4B (Bottinelli et al., 2007). Each of these sources was further analysed in other studies to get a broader sense of the chemical interior of such sources. These initial detections of hot corinos were followed up in 2016 by Codella et al. with the detection of the first hot corino in Orion, where $CH_3CHO$ and HDO emission was detected in the inner ~100 AU of HH212. In the same year saturated COMs were detected in the inner regions of the low-mass Class 0 protostar IRAS 19347+0727 in the Bok globule[2] B335 by Imai et al. (2016). Other sources found in the last years are L483 (Oya et al., 2017), Barnard 1b-S (Marcelino et al., 2018), Ser-emb 1 (Martín-Doménech et al., 2019) and BHR71-IRS1 (Yang et al., 2020).

Hot corino signatures were also found towards more evolved protostars in the Class I stage. These include B1a (Öberg et al., 2014), NGC 1333 SVS13A (De Simone et al., 2017) and Ser-emb 17 (Bergner et al., 2019). Another interesting detection of a hot corino was made in 2018. Ospina-Zamudio et al. (2018) detected a hot corino around the intermediate mass protostar Cep E-mm, where one of the binaries of this source showed clear hot corino properties.

The hot corino source SMM1a, which is the main focus of this thesis was first thought to be a single source, but later revealed itself to be a binary system, just like other similar sources which were mentioned in this section, like NGC 1333 IRAS 4A, NGC 16293-2422 and Cep E-mm. This multiplicity of low mass Class 0/I protostars was also found by Maury et al. (20014), who found that 40-60% of protostars are multiple systems. These sources of a binary often show a strong chemical differentiation and only one component being associated with a hot corino, like in the case of Cep E-mm and NGC 1333 IRAS 4A.

[2]Bok globules are isolated and relatively small dark nebulae, containing dense cosmic dust and gas from which star formation may take place.

In the last ~20 years 10 Class 0 and 3 Class I protostar hot corinos were observed and identified. This can be attributed to observations of such sources getting better and more COM being identified in their vicinity. De Simone et al. (2017) also showed that about 30% of low mass Class 0/I protostars show emission from at least three COMs.
In the hot vicinity of the young protostar for the first time since them freezing onto dust grains COMs are desorbed into the gas phase, meaning they can give us some clues about the conditions shortly before the pre-stellar core collapse where they froze out. Through studying hot corinos the questions how, when and where COMs and potentially prebiotic molecules [3] are formed could be answered.

## 1.4 Protoplanetary binary SMM1

The protostellar binary SMM1[4] lies within the Serpens main molecular cloud shown in figure 1.2, which is an active star forming region with a complex network of self-gravitating filaments. It is located at a distance of 436 $\pm$ 9 pc (Hull et al., 2017) and contains 34 Class 0 and Class I protostars (Dunham et al., 2015). Within this cloud SMM1 is the brightest millimeter wavelength source and was found to be multiple star system consisting of SMM1a and SMM1b in 2009 by Choi. The two sources have a separation of 500 AU and later in 2017 Hull et al. found that SMM1b is likely to be a binary with a separation of 130AU, with one of these components launching an extremely high- velocity mono-polar jet visible both in CO (J = 2 $\rightarrow$ 1) and SiO (J = 5 $\rightarrow$ 4). In this study they also discovered two other, but weaker compact sources towards SMM1, called SMM1c and SMM1d. SMM1 is associated with several jets and outflows. In 2016 Hull et al. identified high velocity (~80 km/s) CO (J = 2 $\rightarrow$ 1) jets coming both from SMM1a and SMM1b. They also reported a C−shaped extended structure around SMM1a, which they interpret as walls of cavity carved by precession of the jets. Both jets are mono-polar, which could be due to the geometry of the surrounding cloud, but their origin is still not clear (Hull et al., 2016). The sources also fuel bipolar outflows, which were clearly identified into two distinct outflows by Dionatos et al. (2014), one driven by SMM1a and one by SMM1b.

[3] Prebiotic molecules are for instance glycine and glycolaldehyde and are categorized as COMs. They are said to be precursors to the origin of life. (Gargaud et al., 2015)

[4] SMM1 has also been called Serpens FIRS1, Serp-FIR1, S68 FIRS1, Ser-emb 6, S68 FIR, S68-1b and IRAS 18273+0113.

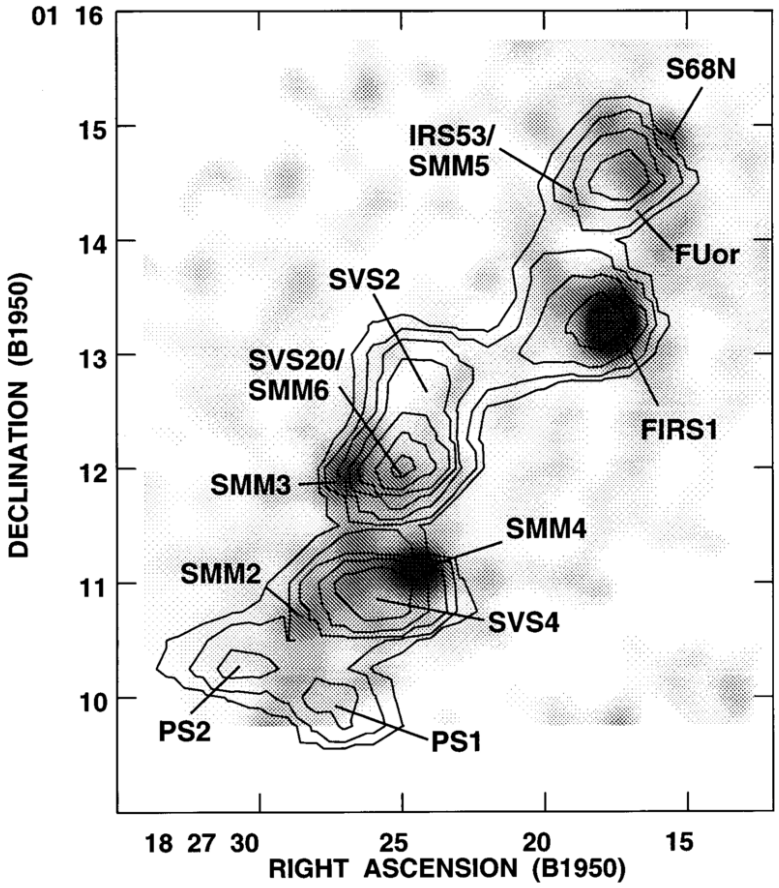


Figure 1.2: Continuum emission map showing the Serpens star forming region, with some of the YSO sources including FIRS1 (SMM1).
Image credit: Hurt & Barsony (2009)

## 1.5 Fractionation

Isotopic fractionation refers to the chemical process of incorporating isotopes[5] with a different mass into a molecule, due to zero-point energy effects (Gargaud et al., 2015). Each isotope in a molecule has a different zero-point energy, which is defined by its vibrational frequency, which depends on its mass (Clark, 1998). Through fractionation the ratio of one isotope to another can alter, showing an enrichment or depletion of one isotope. The zero-point-energy differences between for instance D and H can lead to molecules having an energetic preference to include D atoms at the expense of H atoms, as D atoms are heavier and thus have a lower zero-point energy (Millar, 2005).

[5]Isotopes have different masses due to containing different numbers of neutrons.

The two most common fractionation processes are thermodynamic/equilibrium and kinetic fractionation. The first one depends on equivalent forward and backward reaction rates, so that chemical equilibrium is kept. Kinetic fractionation takes a different route, where the equilibrium is displaced and unidirectional reactions are favoured, which are prominent in biological processes (Clark, 1998). Other fractionation processes are referred to as mass-independent and show most noticeable effects for O and S. The cause for this process to occur is not yet agreed upon, but could lie in the symmetry, spin-orbit coupling, self-shielding or finite volume of heavy nuclei of the isotopologues (Gargaud et al., 2015).

### 1.5.1 Deuteration

Deuterium was formed in the Big Bang and has since then been destroyed through astration, meaning it is burnt to form helium during the lifetime of stars. This indicates that since the Big Bang the ratio of deuterium to hydrogen has been reduced by a factor of 2-3 in the solar neighbourhood (Millar, 2005). As it is formed in the beginning of our universe, the D/H ratio can also be used to give constraints on Big Bang models. This isotope gives an important tool to understand the early chemical evolution of star formation. Therefore the ratio could give some indications on the late stage of cloud collapse, when most gas phase molecules are frozen out on the surfaces of interstellar grains.
The D/H ratio is lower for high-mass protostellar objects as compared to the one of low-mass protostars (Jørgensen et al., 2020). The enhancement in these low-mass sources is around 100 times the cosmic ratio (Millar, 2005). This means that for a hot environment like a hot corino a higher D/H ratio is thought to be present. The D/H ratio for different species and objects are obtained by comparing the deuterated to the non-deuterated form of a species. Such deuterated species, for instance doubly deuterated formaldehyde, form either through hydrogen addition reactions on the surface of dust grains, through subsequent substitution reactions involving D–atoms or through abstraction[6] and addition reactions (Persson et al., 2018).
In a broader context the D/H ratio of solar system objects may also give some clues about the water transport to our Earth as for instance the ratio of Earth coincides with those of a Jupiter family comet and also a carbonaceous meteorite, which are believed to originate from the outer asteroid belt.

[6] An abstraction reaction is the removal of an atom from a molecule by a radical.

## 1.6 Observation

In radio astronomy the natural radio emission from various sources is being studied, as nearly everything emits radio waves at some level. Some sources like the earlier mentioned protostars are obscured by their envelope and as such can only be observed using radio telescopes.

### 1.6.1 Spectral Windows

In terms of the observation of an astronomical object the term of a spectral window is used, meaning that for a certain frequency range the radiation is not absorbed by the atmosphere to a noticeable extent. The Earth's atmosphere absorbs electromagnetic radiation at most infrared (IR), ultraviolet, X-ray, and gamma-ray wavelengths, so only optical/near-IR and radio observations can be made from the ground as shown in Figure 1.3. The radio window is quite broad ranging from about 15 MHz to about 1 THz. The lower frequency limit for ground-based radio astronomy occurs due to the Earth's ionosphere, where free electrons absorb electromagnetic radiation. This lower limit is variable and depends on the density of the ionosphere, which depends on the solar activity. So only observations well above this limit are not effected by the ionosphere. The high frequency cut-off occurs due to the resonant absorption of the lowest rotation bands of molecules in the troposphere, mainly by water vapor and $O_2$. To minimize the effect of the absorption of $H_2O$ observations take place at high altitudes, where the air has a low total water vapor content (Rohlfs & Wilson, 1999).
Within this range almost all types of astronomical sources, thermal and non-thermal radiation mechanisms, and propagation phenomena can be observed at radio wavelengths. To cover the radio window effectively a wide variety of radio telescopes and observing techniques are needed. Some of the major discoveries of radio astronomy include the cosmic microwave background radiation from the hot big bang (Partridge & Wilson, 1965) and the supermassive black hole at the galactic center (Balick & Brown, 1974).

### 1.6.2 Interferometry

Observing within the radio frequency range is possible by using single-dish radio telescopes, but they have a relatively low angular resolution and pointing accuracy, small field-of-view (if the antenna is big) and limited sensitivity (Condon & Ransom, 2018). So far the largest single-dish radio telescope is FAST (Five-

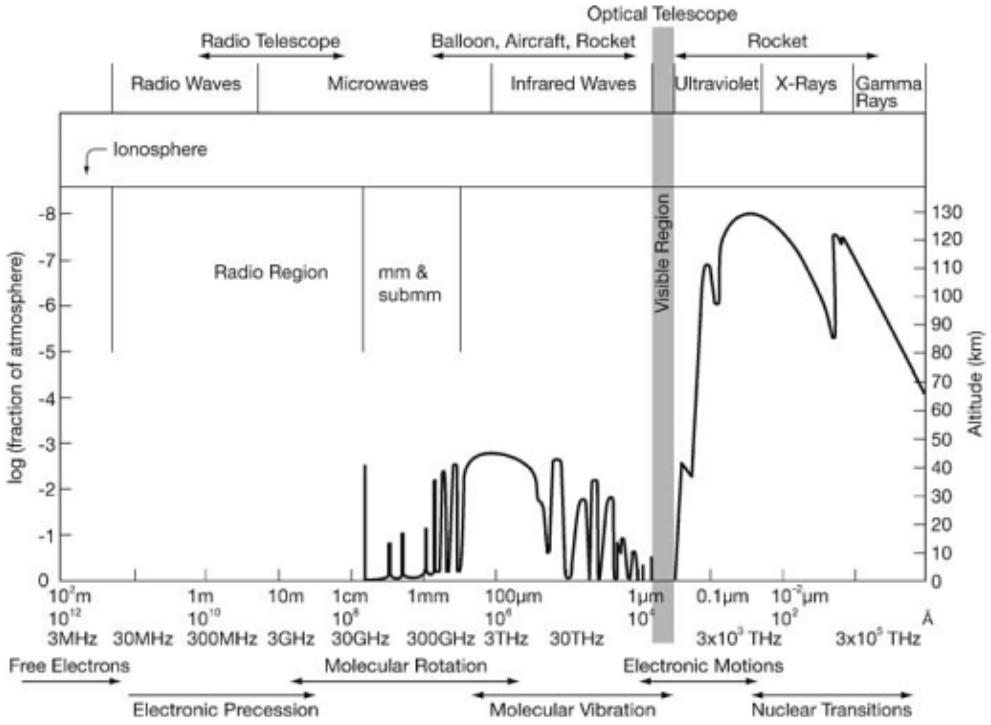


Figure 1.3: Here the different atmospheric windows are shown, with the radio window being the broadest one.
Image credit: Rohlfs & Hüttemeister (2009)

hundred-meter Aperture Spherical Radio Telescope)[7] with a diameter of 500 m. This shows that to achieve high resolution observations in radio wavelengths with single-dish telescopes extremely large diameters are needed, where the geometric area is $\pi R^2$ (with R being the radius of the dish) and the angular resolution $\approx \lambda/D$ ($D$ being the diameter of the dish). An interferometer can increase this area by using N dishes with a total collecting area of $N\pi R^2$ and also the angular resolution $\approx \lambda/b$ ($b$ being the baseline), so the angular resolution of an interferometer can be much higher than for a single dish telescope as it depends on its baseline (the maximum separation between two antennas). This in turn reduces some of the problems with single-dish observation, such as the vulnerability to fluctuations in atmospheric emission and receiver gain, radio-frequency interference, and pointing shifts caused by atmospheric refraction.
The simplest radio interferometer is a pair of radio telescopes whose voltage outputs are correlated (multiplied and averaged). Interferometers with a number of antennas N contain $N(N-1)/2$ pairs of antennas, each of which is a two-element

[7] http://english.nao.cas.cn/

interferometer. A basic scheme of such a telescope is shown in Figure 1.4, where two antennas are separated by the baseline $\vec{b}$, the direction of a distant source ŝ, the voltage outputs of the antennas $V_1$ and $V_2$. The geometric delay of the two antennas $\tau_g = \vec{b} \cdot \hat{s} / c$ causes interference fringes for one of the antennas. The contrast of the fringes and the phase delay correspond to the *complex visibility* (R) (Mary et al., 2013), which varies due to the Earth's rotation, as the source direction changes relative to the baseline (Condon & Ransom, 2018). This is then further reduced, shown in the reduction process in section 2.2, where through a inverse Fourier transform a 'dirty' image is computed (Mary et al., 2013).

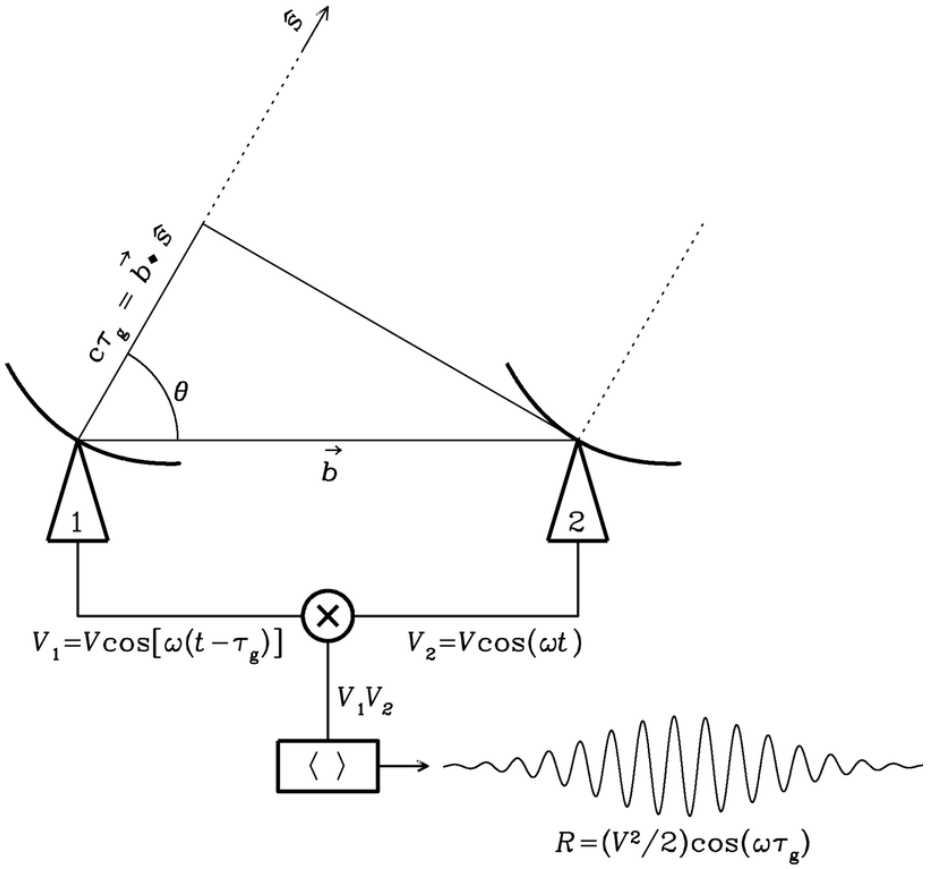


Figure 1.4: The scheme for the simplest radio interferometer with a pair of radio telescopes. Image credit: Condon & Ransom (2018)

The primary beam of an interferometer is the beam of any single antenna and is determined by the diameter of the single antenna dish. It also called the power pattern, can be improved by increasing the number of antennas and in turn increasing the number baselines (Figure 1.5).

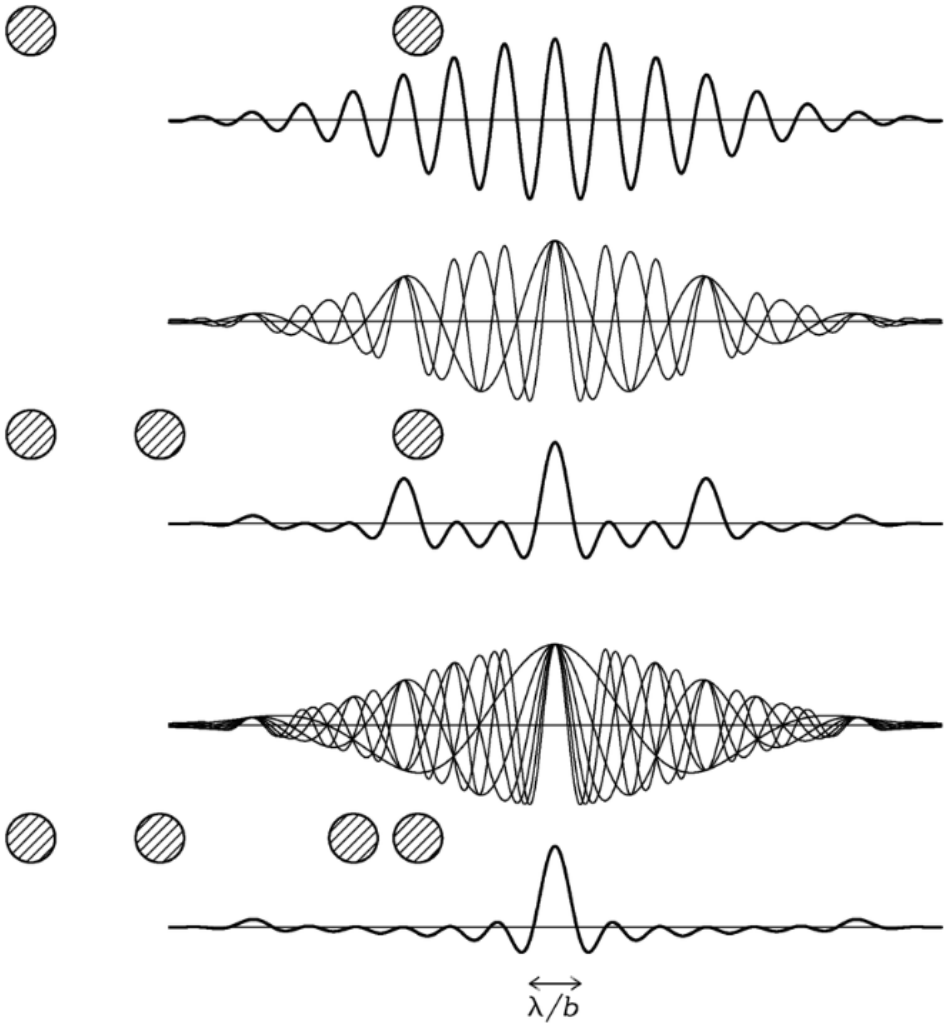


Figure 1.5: The instantaneous point-source responses of interferometers for two, three and four antennas are shown by the thick curves. The thin curves correspond to the individual responses of the two-element interferometers, so for each baseline. (Condon & Ransom, 2018)
Image credit: Condon & Ransom (2018)

Interferometers are not only used in radio astronomy but also cover near infrared and optical wavelengths, for instance the VLTI (Very Large Telescope Interferometer), where 4 fixed 8.2 m and 4 movable 1.8 m antennas work as an interferometer with a maximal baseline of 140 m. The 4 8.2 m telescopes can also be used individually. Optical interferometry comes with the problem of the effect of turbulence due to the atmosphere. The temperatures of the different layers of the atmosphere differ and through convection turbulences occur. This leads to the local wavefront being corrugated and to fluctuations of the optical path

differences for each baseline.

### 1.6.3 ALMA telescope

The Atacama Large Millimeter/submillimeter Array (ALMA) is located at one of the highest and driest places on Earth, the Chajnantor Plateau in the Atacama Desert. It consists of 66 antennas, with a main array of 54 12-meter antennas, which act as an interferometer and can be arranged in configurations spreading over distances from 150 m to 16 km. The compact array configuration consisting of four antennas with 12-meter diameters and 12 antennas with 7-meter diameters. The compact array has two configurations, one of which is a north-south extension to provide a better coverage of sources that are either very far north in the sky or very far south.
Observations with ALMA give insight into places where visible observations show nothing and give information to study the chemical and physical conditions for such objects, like protostars and molecular clouds. ALMA observations are conducted within 10 different bands with frequency ranges of 31-45, 67-86, 86-115, 125-163, 163-211, 211-275, 275-373, 385-500, 602-720 and 787-950 GHz, covering the mm- and submm range spectral windows.
In the context of astrochemistry the usage of a high sensitivity telescope like ALMA gave some great advancements in the last years. Since it has been in operation around 40% of all new COMs detections were made with ALMA (Jørgensen et al., 2020).

Figure 1.6: View of the ALMA antennas.
Image credit: P. Horálek (ESO)

# Chapter 2

# Data Analysis

This chapter focuses on the processes used for determining the results which are presented in section 3 and are further put into context in section 4. The first section describes the analysed datasets and their parameters. The following sections concentrate on the used processing and post-processing tools, CASA and CASSIS, where the basic data reduction and line identification process is presented. The usage of excitation diagrams and synthetic spectra is also demonstrated. At last the calculation of the abundances for the different species and the deuterated isotopologue of formaldehyde is presented.

## 2.1 Observations

SMM1 was observed with the ALMA telescope as part of the 'The dynamics of molecular gas in outflow shocks' project by PI M. Persson. The observations were carried out in September 2018 and cover the ALMA Band 6 frequency range of 211-275 GHz with a sensitivity of 3.5 mJy and an achieved beam size of 0.408"x0.318". The analysed dataset covers 218.057-219.930 and 230.279-232.179 GHz. To get a broader spectral range the lower frequency range was extended by using observations from 2015 of the 'Imaging the circumstellar matter around Class 0 protostellar binary SMM1/FIRS1 in Serpens' project by PI O. Dionatos. This data overlaps with the 2018 data but adds a range of 217.562 - 218.062 GHz, has an achieved beam size of 0.30"x0.25" and a sensitivity of 3.5 mJy. The fluxes for the 2015 data are lower by 17% compared to the 2018 data. The absolute uncertainty on the flux calibration is set to 17% for all calculations.

## 2.2 CASA

The data coming from the ALMA telescope are commonly reduced and analysed using CASA (Common Astronomy Software Application)[8]. This processing tool is used by radio telescopes like ALMA, VLA, VLBA, and ATCA, so it is able to process interferometric data, but could also be used for single dish data. Apart from data reduction CASA can also be used to analyse spectra from a specific region. By using this tool different spectra can be extracted from the dataset. This spectrum can be analysed going through each channel and searching for possible species within a certain frequency range. This process is shown and described in the screenshots 2.1 and 2.2.
This line identification process does not always lead to a definite species detection, as often an overlap with other species with similar frequencies is present. For transitions which could not be clearly attributed to a specific species a further investigation was made using CASSIS.

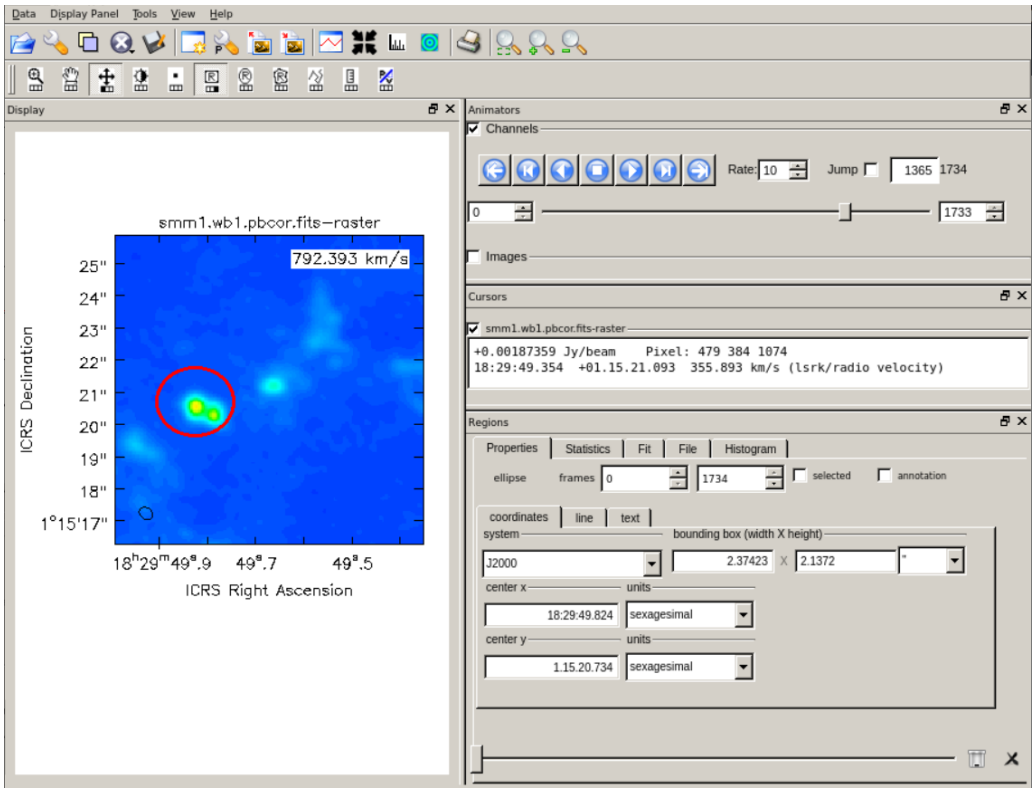


Figure 2.1: Screenshot of the CASA viewer display panel. The red circle shows the region from which the spectrum is extracted from.

[8] https://casa.nrao.edu/

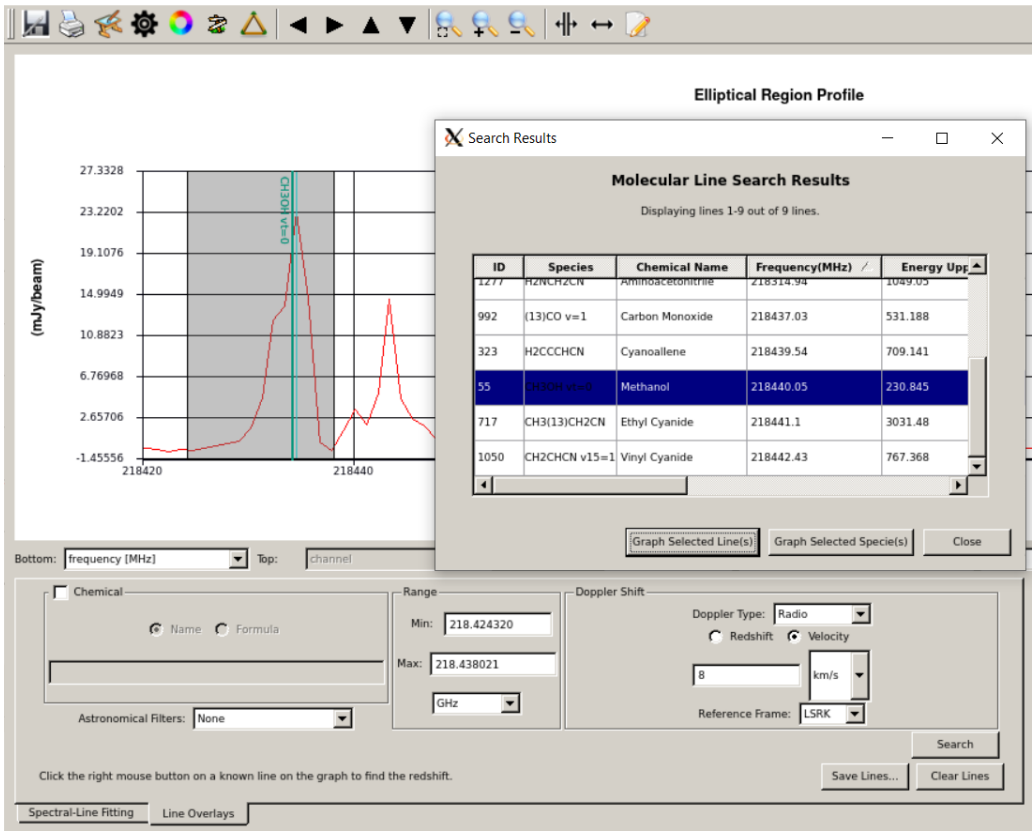


Figure 2.2: Here the gray region in the spectrum gives the frequency range in which possible transitions are searched for. In the small panel on the right some of the found transitions within this range are shown. In this case the identified line is the $CH_3OH$ line at 218.44 GHz.

### 2.2.1 Reduction process

The basic data reduction process proceeds from data examination and editing, calibration to imaging, with the final goal of an image for further investigation. The basic process is shown in figure 2.3, where at first the data needs to get imported and then examined. At this step information like the observed target, the observation time range, the used antennas and the spectral setup (spectral windows and channels) is gathered. The next step is to do a priori flagging, where 'shadow' data, meaning data where one antenna blocks the line of sight of another one is excluded. Scans that were used to carry out pointing and atmospheric calibration and autocorrelation data (the combination of the signals of each antenna with itself, but are not needed once the system temperature and Water Vapour Radiometer (WVR) tables are computed) are flagged.
After the first flagging process the calibration comes next. At first the system

temperature, the Water Vapour Radiometer and the antenna positions are calibrated. Through the system temperature calibration the contribution of atmospheric ozone absorption lines are minimized. The WVR calibration concentrates on the phase delay due to the atmospheric water line and tries to compensate this effect. The antenna positions get updated and refined from their measured positions. After applying these calibrations, the data has to be inspected on the effects of the calibration and if further problems like missing data occurs, they have to be taken into account.
The next calibration step is to do a bandpass, flux and phase calibration. The bandpass calibration's purpose is to track the variation of the instrumental response at different frequencies. For the flux and phase calibration a calibrator is needed for referencing to obtain a reliable absolute flux measurement and to take the phase and amplitude behavior of the antennas into account. The flux calibrator should be a bright source with known flux and the phase calibrator one with a well known position. The flux calibrator for both the data from 2018 and the one from 2015 is the source J1751+0939. The phase calibrator was J1830+0619 for both datasets. Here the data should be inspected again and if necessary the steps repeated.
The last step in the data reduction process is imaging, where from the calibrated data an image is computed that can be analyzed. At first for spectral line data the continuum emission can be subtracted. The next step is to generate a so-called 'dirty' image by applying a simple gridded Fourier inversion of the calibrated data. Then a model image is reconstructed from the interferometric data. Further steps can include self calibration, where the model image is used to further refine the calibration of the target source.
The reduction for the two datasets was not part of this master's thesis and I was provided with images, which could be analysed.

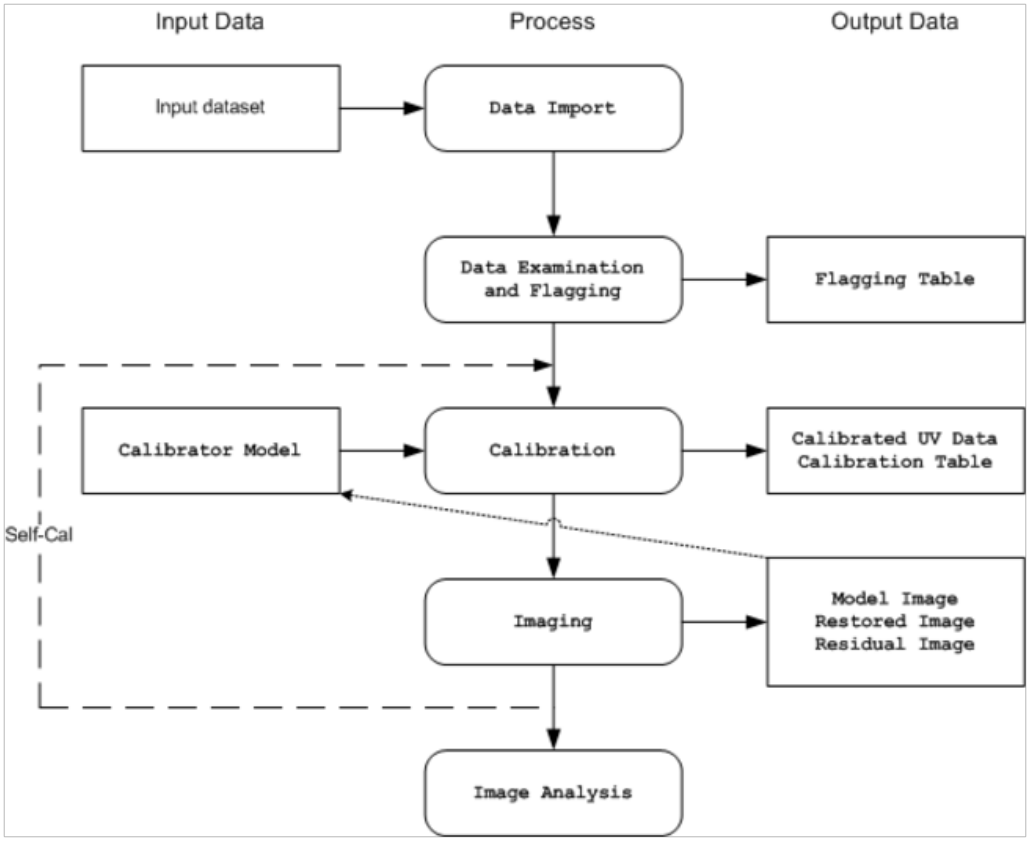


Figure 2.3: Showing the basic data reduction process. The different steps can be summed up by: importing, examining, calibrating and imaging.
Image credit: https://casa.nrao.edu

## 2.3 CASSIS

CASSIS (Centre d'Analyse Scientifique de Spectres Instrumentaux et Synthétiques)[9] is a free interactive spectrum analyser, where line fitting, synthetic spectra and excitation diagrams can be produced.

### 2.3.1 Line identification

As mentioned at the end of section 2.2, for some lines a clear identification could not be obtained with CASA. The spectra have to be imported into the program, where we realize that CASSIS uses other units for the intensity and flux of a line than CASA: in CASA Jy/beam and in CASA Kelvin is used. Due to that difference in units when importing the CASA spectra the achieved beam size

[9] http://cassis.irap.omp.eu/

according to the dataset has to be taken into account. This can be done within CASSIS as it asks for data in different units than Kelvin for the major and minor beam sizes. Another approach is through a code (which I was provided with) which adjusts the units the the format of the data.
The first step in the identification process is to show all the probable species and compare them to the spectra and their fit. The shown species can be limited using an upper energy level ($E_{up}$), also the velocity shift can be set (here to 8km/s, obtained through calibration of the spectra with the most prominent CO transition) and each species can be individually displayed. At first a reasonable upper energy level which depicts most of the transitions has to be found. For this I started by fitting the strongest lines and through that got an upper energy level of up to 300 K. As a next step I searched for species with $E_{up} \leqslant 300$ K for all the lines to find fitting transitions. This search for a specific species for this upper energy level is shown in figure 2.4. For some of the lower transitions a higher upper energy level was needed. This range of $E_{up}$ in combination with the strength of the transition shows itself in the Boltzmann distribution of the transitions, also shown in section 2.4, where the transitions with a lower flux have a lower upper energy level.
The transitions can be fitted with a simple Gaussian and the parameters of the fit saved. One of the $CH_3OH$ transitions shown in figure 2.4 is fitted with a Gaussian fit as an example in figure 2.5. Although the fitting of the spectrum in combination with the possible transitions lead to more clearly identified species, still some blended lines (multiple identification for one transition) are present. To narrow it down more these transitions are further investigated using synthetic spectra.

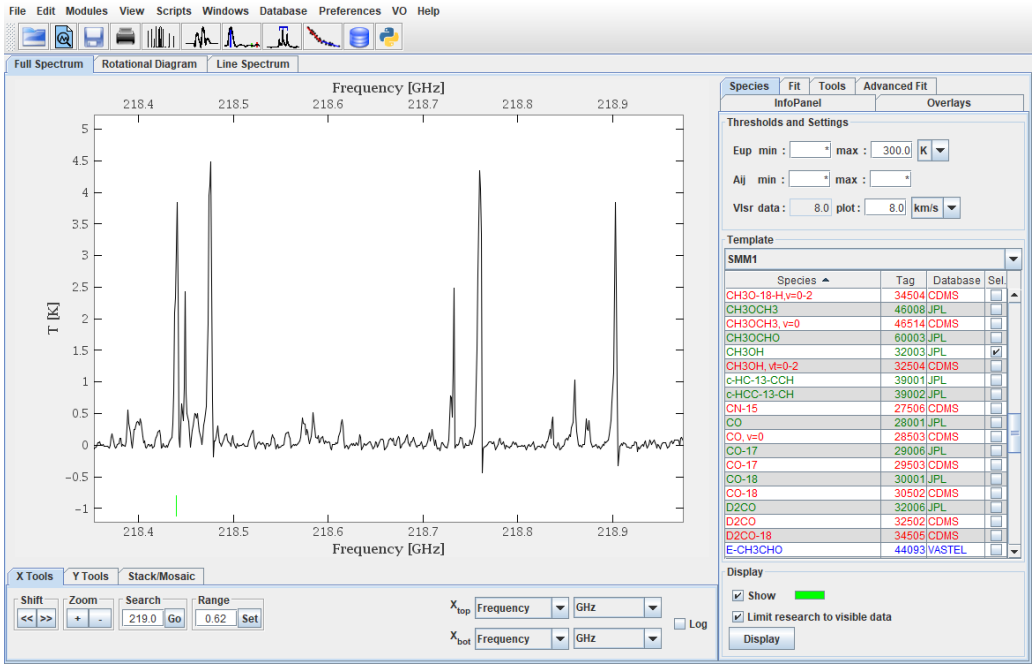


Figure 2.4: A screenshot of CASSIS with the spectral range of 218.35 - 218.95 GHz is displayed. On the right hand side the different parameters for the species/-transitions search is given. There are also the possible species listed. In this case the search was limited to $CH_3OH$ and $E_{up} \leqslant 300$ K. There is one transition found for this species, indicated by the green line on the lower end of the spectrum panel.

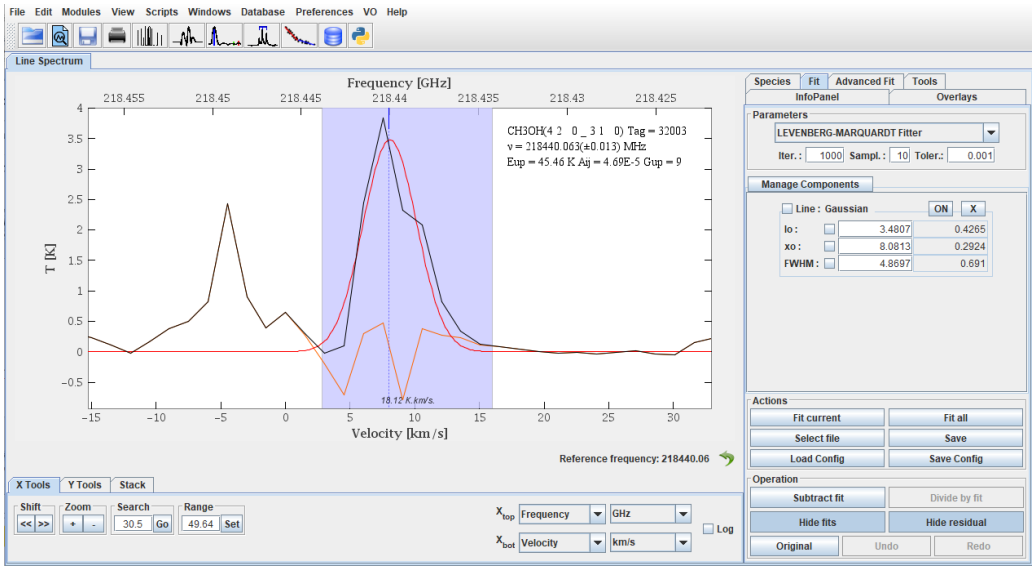


Figure 2.5: The fitted $CH_3OH$ transition at 218.44 GHz. On the smaller panel on the right, the parameters of the fit are displayed.

## 2.4 Excitation Diagrams

Excitation diagrams are also referred to as population or rotational diagrams and give a tool to easily determine the column density and the excitation temperature of a molecular species. The diagram plots the energy above the ground state ($E_{up}$) against the column density per statistical weight ($\ln(N_u/g_u)$). This is approached by assuming that all transitions are optically thin and thermalized and local thermodynamic equilibrium (LTE) upholds, which corresponds to a Boltzmann distribution (Goldsmith & Langer, 1999).
These assumptions, calibration errors and the assumption of a Gaussian line profiles in the fitting process can lead to errors in the diagram's outcome. If the transitions are not completely thermalized this leads to deviations from linearity. If the emission is not optically thin the plot will not display a linear fit but an increased scatter of the data points. As a result the calculated total column density will be underestimated. Errors in the estimated fluxes and also in the intensities can occur due to lines not properly fitted. Non-linear molecules, meaning more complex molecules, have a more complex energy level structure and can as a result increase the mixture of optically thin and thick lines (Goldsmith & Langer, 1999).

For the calculation of the parameters CASSIS can be used, where the line fitting can be done. The parameters of the individually fitted transitions can be saved and with them excitation/rotational diagrams computed. The data points within the diagram can be fitted to a straight line, when plotting $\ln(N_u/g_u)$ against $E_{up}/k$. Through that the excitation temperature and column density of a species can be calculated. An example of an excitation diagram computed with CASSIS is shown in figure 2.6. The parameters for the calculation were taken from the fitting of each transition, as shown in section 2.3.1 and figure 2.5.

The calculation itself needs an equation with the mentioned parameters. We start with the equation of radiative transfer, which describes the change in the intensity of a source emitting along a line of sight $I_\nu$ through radiation being absorbed or emitted. The solution of the equation of radiative transfer in the optically thin limit gives:

$$I_\nu = \int \epsilon_\nu ds = \frac{h\nu_{ij}}{4\pi} A_{ij} \int n_i ds \tag{2.1}$$

In principle, for a molecule in LTE the excitation temperatures of all transitions

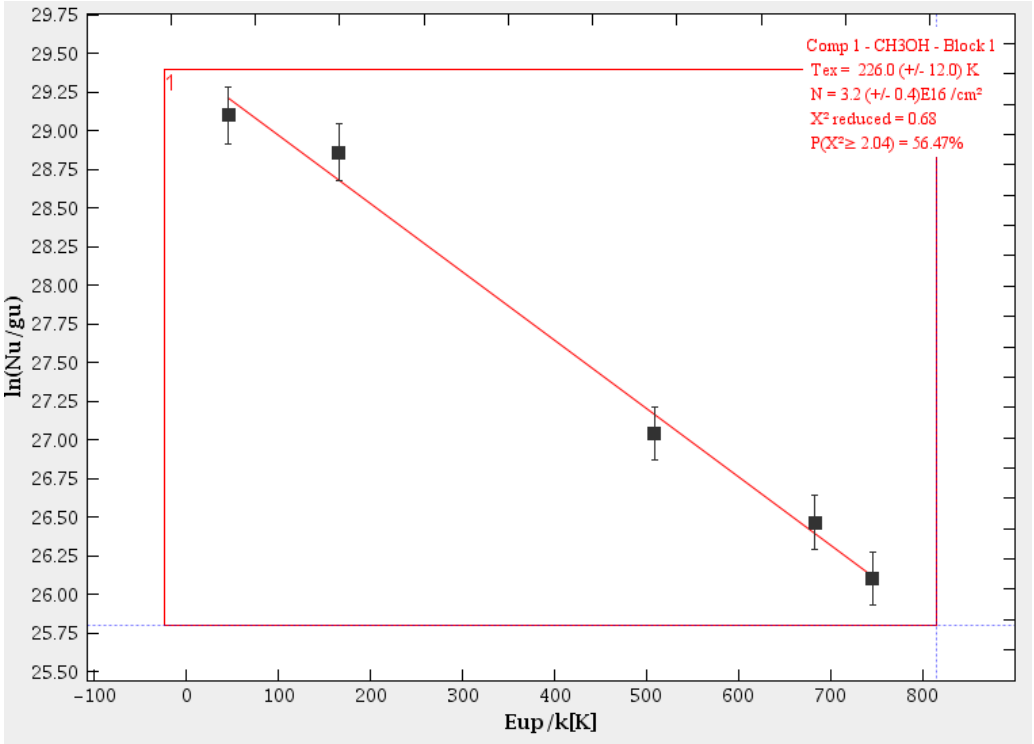


Figure 2.6: The excitation diagram for $CH_3OH$ computed by CASSIS.

of one species are the same, the population of each level is given by:

$$\frac{N_i}{N_{tot}} = \frac{g_i}{Z} e^{-E_i/kT_{ex}} \tag{2.2}$$

Combining equations 2.1 and 2.2, where $N_i = \int n_i ds$, gives the basic equation:

$$ln\frac{N_i}{g_i} = ln\frac{4\pi I_i}{h\nu g_i A_i} = -\frac{E_i}{kT_{ex}} + ln\frac{N_{tot}}{Z} \tag{2.3}$$

The individual parameters of the equation include the column density of an individual transition $N_i$, the statistical weight $g_i$, the intensity of the transition $I_i$, planck's quantum of action $h$, the frequency of the transition $\nu$, the Einstein coefficient $A_i$ (giving the probability of a spontaneous transition per second within a volume), the upper energy $E_i$, the excitation temperature $T_{ex}$, the partition function $Z$, the Boltzmann constant $k$ and the total column density of the molecular species $N_{tot}$.

The excitation temperature is calculated through the slope of the fit, which is given by $1/T_{ex}$. To calculate the total column density of the molecular species the $ln\frac{N_{tot}}{Z}$ term has to be determined. This can easily be done as it is the point where

the linear fit intersects with the y-axis, implying that $E_i = 0$ equation 2.3 becomes:

$$ln\frac{N_i}{g_i} = ln\frac{4\pi I_i}{h\nu g_i A_i} = ln\frac{N_{tot}}{Z} \tag{2.4}$$

Now only the partition function ($Z$) is missing, which gives the sum over the states of a molecule. The used partition functions for the calculation are taken from the CDMS (Cologne Database for Molecular Spectroscopy)[10] and the JPL (Jet Propulsion Laboratory)[11] catalogue. The partition function is given by the relation:

$$Z = \sum_i g_i \cdot n_i = \sum_i g_i \cdot e^{-E_i/kT_{ex}} \tag{2.5}$$

For species with only two transitions, the approach explained above is not always working, as it can lead to a positive slope, the opposite of what is required for an excitation diagram analysis. In the case of $D_2CO$ this is the case, where only two transitions are identified. With the requirement that the upper energy levels differ between the two transitions the following equation can be used for the excitation temperature (Favre et al., 2015):

$$T_{ex} = -\frac{h\nu}{k \cdot ln\left(\frac{g_l A_l \nu_u^2 W_u}{g_u A_u \nu_l^2 W_l}\right)} = -\frac{E_u - E_l}{ln\left(\frac{g_l A_l \nu_u^2 W_u}{g_u A_u \nu_l^2 W_l}\right)} \tag{2.6}$$

where $W$ denotes the integrated line intensity. Now that we have a simple equation for the excitation temperature calculation, the column density can be calculated using:

$$ln\left(\frac{8\pi k \nu^2 W}{g_u h c^3 A_{ul}}\right) = ln\left(\frac{N_{tot}}{Z}\right) - \frac{E_u}{T} \tag{2.7}$$

[10] https://cdms.astro.uni-koeln.de/
[11] https://spec.jpl.nasa.gov/

## 2.5 Synthetic spectra

The synthetic spectra are calculated assuming that for the excitations LTE applies, meaning that all transitions are thermalized. The parameters needed to compute a synthetic spectrum are the column density, the width of the line, the excitation temperature, the size of the source and the LSR (local standard of rest) velocity. The source size was taken from the beam size of 0.408" x 0.318" and set to 0.363". This parameter as well as the width of the line (4.5km/s), the LSR velocity (8km/s) and the excitation temperature of 200K were fixed for all the molecules. For the excitation temperature and the line width methanol was used as a template to set these parameters, as it is the first COM to form on the grains' surface. The column densities for each molecule were earlier calculated using excitation diagrams. Here again a certain threshold for the upper energy could be set as a further constraining factor. The synthetic spectra could be computed for each individual species, but also for all prominent species (where enough transitions for an excitation diagram calculation were identified) at once.
The synthetic spectrum was now compared to the observed spectra to confirm if the LTE model predicts a transition of a species for an observed line. For the lines with multiple possible species mostly only one of the species was predicted in the synthetic spectra and as a result the transition was attributed to this species. This comparison is shown in figure 2.7, where the black line is the observed and the red line the synthetic spectrum. For this transition at 230.31 GHz two species are possible, $CH_3OCHO$ and $CH_3CHO$, but only for the latter the synthetic spectrum predicts a transition. This transition is now identified as $CH_3CHO$.
The outcome of the comparison leads to a clearer identification and as such a more exact column density and excitation temperature calculation. The identification process still leaves some species blended with other species, as they have similar frequencies and are also within the LTE model predictions and as such these transitions have to be left out of the calculation process.

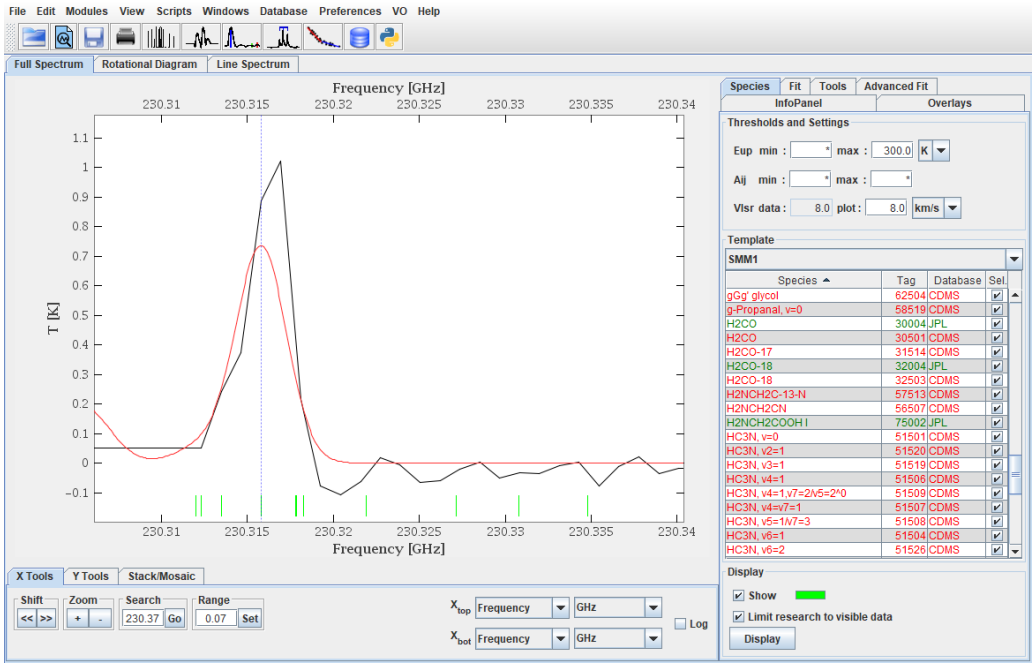


Figure 2.7: The comparison of the observed (black) and the synthetic (red) spectrum for the 230.31 GHz transition.

# Chapter 3

# Results

The processes and tools explained in the previous chapter 2 lead to the results presented here. The transitions and species found within the dataset are described, as well as the excitation temperature and column density of each species for SMM1a and SMM1b are shown in tables 3.1 and 3.2. The excitation diagrams for the most abundant species of SMM1a are shown and described individually. The synthetic spectra compared to the observed spectra for SMM1a are included in section 3.3.

## 3.1 Detected lines and species

The analysis of the spectra of SMM1a show 244 identified transitions from 35 different species and isotopologues. For 10 of these species excitation diagrams could be computed, as they have more than 5 clearly identified transitions. The binary partner of SMM1a also shows some clearly identifiable lines, although with only 69 transitions in the same frequency range fewer than for SMM1a. The intensity of the transitions also seems to be weaker. As a result for SMM1b only for five COM could an excitation diagram be obtained. The detected transitions and the observed spectra for SMM1a are shown in figures 3.12 - 3.16.

## 3.2 Excitation diagrams

The calculated column densities and excitation temperatures for the species of SMM1a are shown in table 3.1 and for SMM1b in table 3.2. The used transitions for these calculations are shown in table 5. The calculated uncertainties of the values include the calibration error of 17% as well as the uncertainties during the

fitting process of the spectral lines with a Gaussian fit. The shown and discussed excitation diagrams in section 3.2.1 are calculated using the transitions found towards SMM1a.

| Species | Chemical name | # of lines | $T_{ex}$ [K] | $N_{tot}$ [cm$^{-2}$] |
|---|---|---|---|---|
| Ethylene Glycol | g'Ga-$(CH_2OH)_2$ | 14 | $127.3 \pm 38.8$ | $6.3 \pm 2.5 \cdot 10^{14}$ |
| Acetaldehyde | $CH_3CHO$ | 16 | $197.7 \pm 27.8$ | $1.1 \pm 0.2 \cdot 10^{15}$ |
| Vinyl Cyanide | $C_2H_3CN$ | 10 | $216.2 \pm 25.2$ | $2.6 \pm 0.6 \cdot 10^{14}$ |
| Methyl Formate | $CH_3OCHO$ | 15 | $74.9 \pm 15.9$ | $1.5 \pm 1.5 \cdot 10^{16}$ |
| Isocyanic Acid | HNCO | 5 | $186.7 \pm 23.0$ | $4.1 \pm 0.7 \cdot 10^{14}$ |
| Ethanol | $C_2H_5OH$ | 7 | $172.3 \pm 23.6$ | $3.5 \pm 1.0 \cdot 10^{15}$ |
| Acetone | $CH_3COCH_3$ | 5 | $71.9 \pm 42.0$ | $2.3 \pm 2.2 \cdot 10^{14}$ |
| Cyanamide | $NH_2CN$ | 4 | $209.6 \pm 50.0$ | $3.2 \pm 0.8 \cdot 10^{13}$ |
| Methanol | $CH_3OH$ | 5 | $225.9 \pm 12.0$ | $3.2 \pm 0.4 \cdot 10^{16}$ |
| Formaldehyde | $H_2CO$ | 3 | $191.5 \pm 27.6$ | $4.6 \pm 0.2 \cdot 10^{15}$ |
| Cyclopropenylidene | c-$C_3H_2$ | 6 | $57.9 \pm 8.9$ | $3.3 \pm 0.6 \cdot 10^{14}$ |

Table 3.1: The calculated excitation temperatures and column densities and the number of used transitions for the calculation of the prominent species towards SMM1a.

| Species | Chemical name | # of lines | $T_{ex}$ [K] | N [cm$^{-2}$] |
|---|---|---|---|---|
| Acetaldehyde | $CH_3CHO$ | 7 | $101.7 \pm 156.1$ | $4.3 \pm 7.1 \cdot 10^{14}$ |
| Methyl Formate | $CH_3OCHO$ | 6 | $146.7 \pm 124.4$ | $4.7 \pm 8.3 \cdot 10^{16}$ |
| Isocyanic Acid | HNCO | 5 | $174.5 \pm 10.4$ | $3.3 \pm 0.3 \cdot 10^{14}$ |
| Cyclopropenylidene | c-$C_3H_2$ | 6 | $58.3 \pm 26.3$ | $1.1 \pm 0.6 \cdot 10^{14}$ |
| Methanol | $CH_3OH$ | 5 | $202.5 \pm 46.3$ | $3.0 \pm 1.7 \cdot 10^{16}$ |

Table 3.2: The excitation temperatures and column densities and number of used transitions of the prominent species towards SMM1b.

### 3.2.1 Discussion of the individual species

#### Methanol

Methanol ($CH_3OH$) is the first COM to form on the grains surface via hydrogenation of iced CO by successive addition of H atoms and is as such used as a template for the analysis in this thesis. It has a very similar geometry to water, but with one H being replaced by a methyl group ($CH_3$). The nuclear spins of the three H atoms create the A- and E- symmetry states. In addition there is also torsion between the methyl group and the HO-C framework (Kwok, 2012).
The excitation diagram shows a very nice linear fit, which would indicate that $CH_3OH$ is optically thin, but from previous works methanol has been established

as being optically thick. The outcome of the diagram in this case could indicate that the emission comes from a narrow region, so that the optically thick methanol still upholds the optically thin assumption.

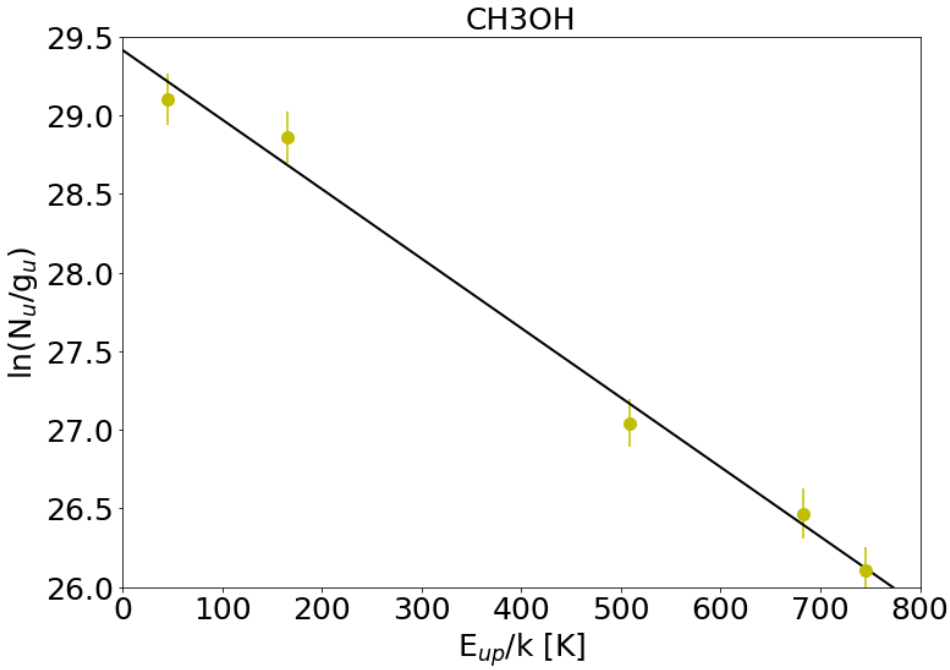


Figure 3.1: The excitation diagram for $CH_3OH$.

**Methyl formate, acetic acid and glycolaldehyde**

The three isomers of $C_2O_2H_4$ are methyl formate ($CH_3OCHO$), acetic acid ($CH_3COOH$) and glycolaldehyde ($CH_2OHCHO$). Methyl formate has been detected in 1975 towards Sgr B2 by Brown et al. (1975) and is typically found towards hot cores, but also hot corinos like the Class 0 protostar IRAS 162937−2422 (Manigand et al., 2019). It is linked to different reaction processes and is not strictly considered to be a prebiotic molecule. It has two internal rotors which lead to the two conformers, cis and trans (Kwok, 2012).
Acetic acid is a prebiotic molecule and is a progenitor in the formation of the simplest amino acid glycine (Burke et al., 2014).
Glycolaldehyde is one of the simplest sugar-like molecules and can, in a reaction with propenal, form ribose, which is a central constituent of RNA (Kwok, 2012). It is one of the four macromolecules essential for all forms of life and has been detected in numerous regions, firstly in Sgr B2 like the other two isomers and

later on in low-mass and high-mass hot cores and also in comets like C/1995 O1 (Hale-Bopp) (Burke et al., 2014). It is the least abundant of the three, with methyl formate being the most abundant according to Hollis et al. (2001).
Unfortunately only for $CH_3OCHO$ a sufficient number of unblended transitions could be identified for an excitation diagram, excluding 7 blended and 4 low amplitude transitions. The used transitions show two clear regimes, differentiated by the their different vibrational state. The less populated regime on the left resides in the ground vibrational state, and the more populated regime on the right has an excited vibrational state. The strong dependence on the ground vibrational state transitions could be the cause of the excitation temperature being lower than compared with temperatures in other studies.

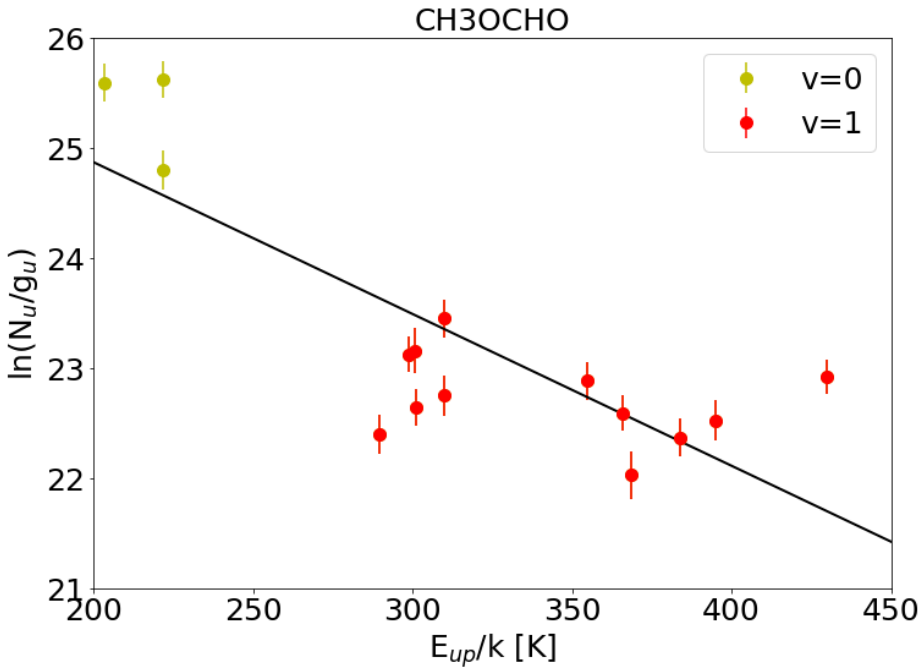


Figure 3.2: The excitation diagram for $CH_3OCHO$ shows the two found vibrational states, with green indicating the ground state and the red dots indicating the excited vibrational state.

### Ethylene glycol

The most abundant species is ethylene glycol (g'Ga-$(CH_2OH)_2$), which is the reduced alcohol version of glycolaldehyde and a triple rotor molecule consisting of two CO bonds and one CC bond. The rotation of these three axes produces

ten different conformers (spatial arrangements). The g'Ga form is designated to the conformer of lowest energy (Kwok, 2012). It was detected in the spectra of comet C/1995 O1 (Hale-Bopp), being the most abundant organic molecule in the cometary ices (Crovisier et al., 2004). The detection of this prebiotic molecule in cometary material could also give some indications on their role in the origin of life on Earth through cometary impacts. Apart from comets it is also identified in both the Murchison and Murray meteorites as the most abundant of the sugar-related alcohols found in such objects (Hollis et al., 2002).
The excitation diagram shows the clearly identified transitions, excluding 6 blended, 8 in LTE under−/overestimated and two with too low amplitudes transitions.

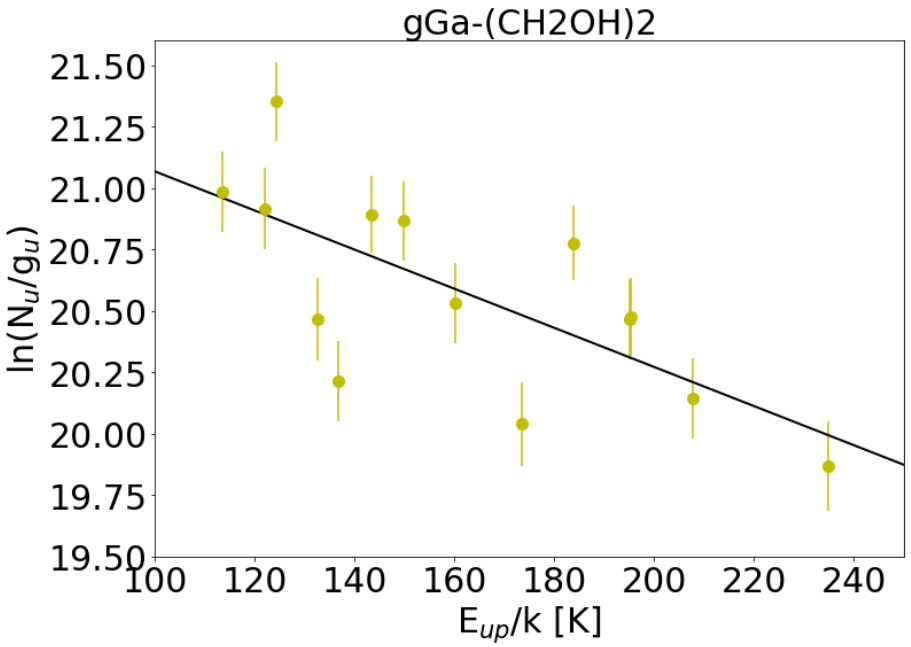


Figure 3.3: The excitation diagram for g'Ga-$(CH_2OH)_2$.

**Acetaldehyde**

The second most abundant species is acetaldehyde ($CH_3CHO$), which is a simple aldehyde. It is an asymmetric molecule, meaning that the nuclear spins of the $CH_3$−(methyl) group lead to either a A- or E- symmetry state (Kwok, 2012). For the calculations no distinction between the symmetry states was made, they also show no clear separation in the excitation diagram. The molecule is of importance as it has a potential role in the formation of amino acids (Occhiogrosso et al., 2014). It could be formed through the combination of the two radicals $CH_3$

and HCO (previously formed by photodissocitation of methanol and formaldehyde, respectively) on the surface of the grains (Garrod & Herbst, 2006).
The excitation diagram of $CH_3CHO$ shows two different vibrational states with a torsional aspect. The excited states correspond to the higher upper energies and for the ground state to the lower energies. The used transitions exclude 9 blended and 4 in the LTE model underestimated transitions.

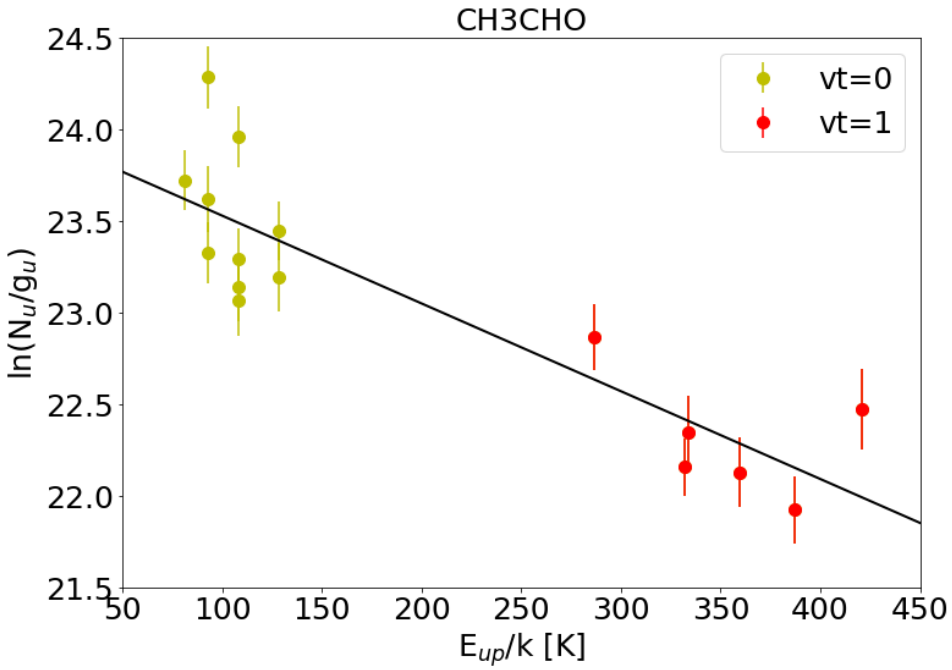


Figure 3.4: The excitation diagram for $CH_3CHO$. The green dots show the ground vibrational torsional state and the red dots the excited vibrational torsional state.

### Vinyl cyanide

Vinyl cyanide ($CH_2CHCN$) was first detected in space towards Sagittarius B2 (Gardner & Winnewisser, 1975) and is one of the simplest olefins. It is a slightly asymmetric prolate rotor which leads to a rich rotational spectrum (Kwok, 2012). In the excitation diagram of $CH_2CHCN$ the scatter to the linear fit is quite small indicating that the used assumptions for the excitation diagram calculation apply. There are 9 blended lines, three transitions underestimated with the LTE model and two lines with a too low amplitude. There are two vibrational states found, the ground state and the excited vibrational state with the C−CN con-

nection being bent. For the different vibrational states the lower upper energy regime is populated by the ground state and the excited vibrational states correlate to the higher upper energies.

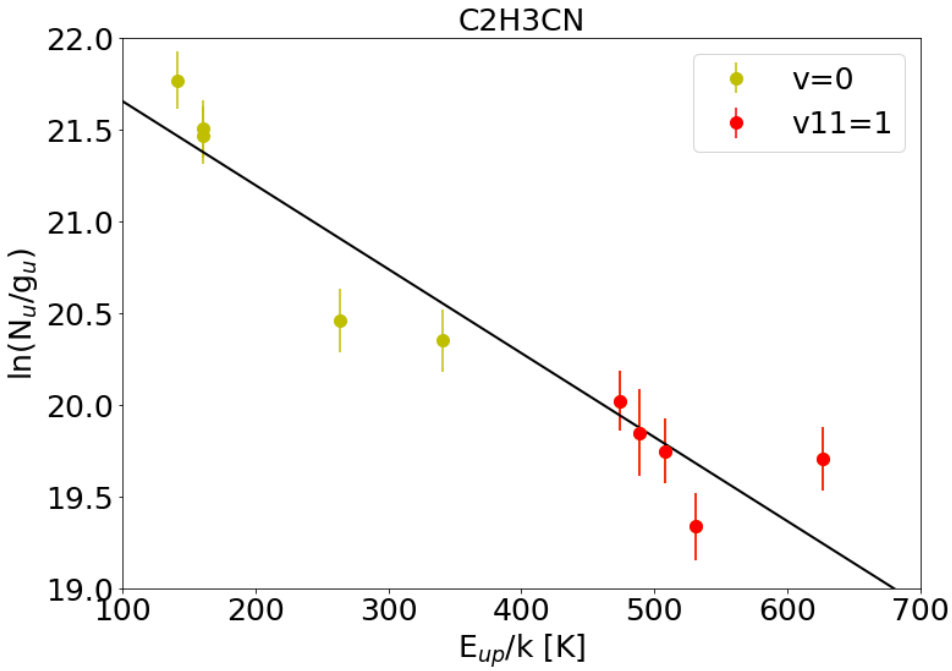


Figure 3.5: The excitation diagram for $CH_2CHCN$. The green dots show the ground vibrational state and the red dots the excited vibrational state.

**Ethanol**

Ethanol ($CH_3CH_2OH$ or $C_2H_5OH$) consists of a $CH_3$-(methyl) group and a OH group which through torsion lead to two conformers, the lower lying anti conformer (trans-) and the doubly degenerate conformer (gauche-) (Jørgensen et al., 2018). The two different conformers are included in the entry and do not show a clear separation.

Three of the identified transitions are blended, three others have an amplitude below the noise and one is very underestimated with the used LTE model. These transitions were excluded from the excitation diagram calculation. The excitation diagram shows a scatter from the linear fit, indicating that the transitions are not optically thin. The transitions also show a wider scatter in their total rotational angular momentum quantum number.

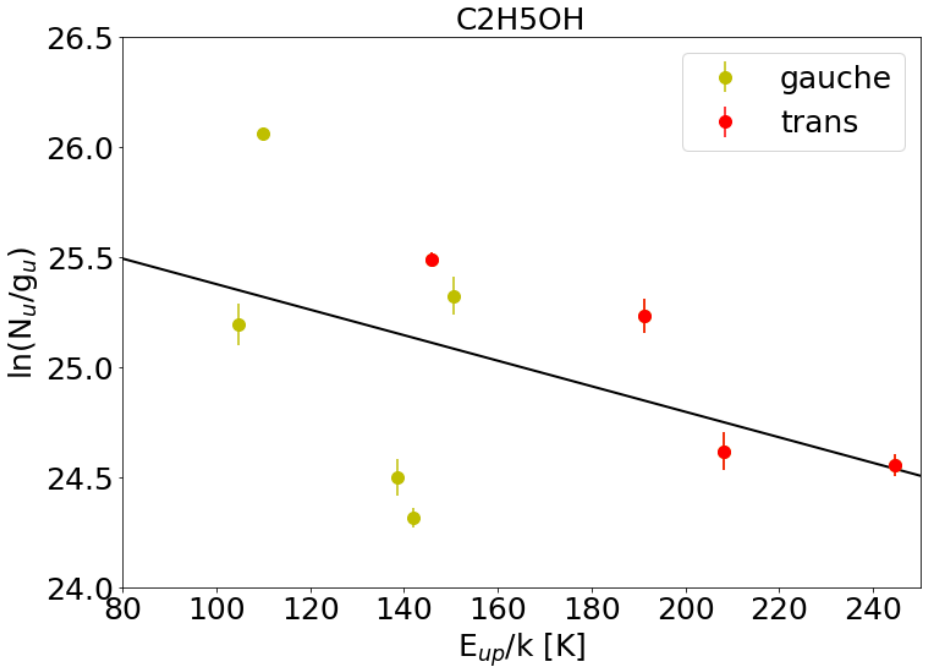


Figure 3.6: The excitation diagram for $CH_3CH_2OH$. The red dots indicate the trans conformer and the green ones the gauche conformer.

**Isocyanic Acid**

Isocyanic acid (HNCO) was first detected in 1972 towards the Galactic center source Sgr B2 by Snyder & Buhl (1972) and as such is one of the first molecules to be detected in space. HNCO is also found in other environments such as molecular outflows and comets. It is the most stable of the simplest molecules, which contain all four atoms essential for life as we know it (Hernández-Gómez et al., 2018). Gathering information about its formation and evolution could add to the models of the organic chemistry in space and especially in star formation regions.

The number of transitions within the used spectral windows is not high, but they are strong and unblended transitions. The assumed LTE model also fits well for those transitions, as the fit to the lines in the excitation diagram follows a straight line.

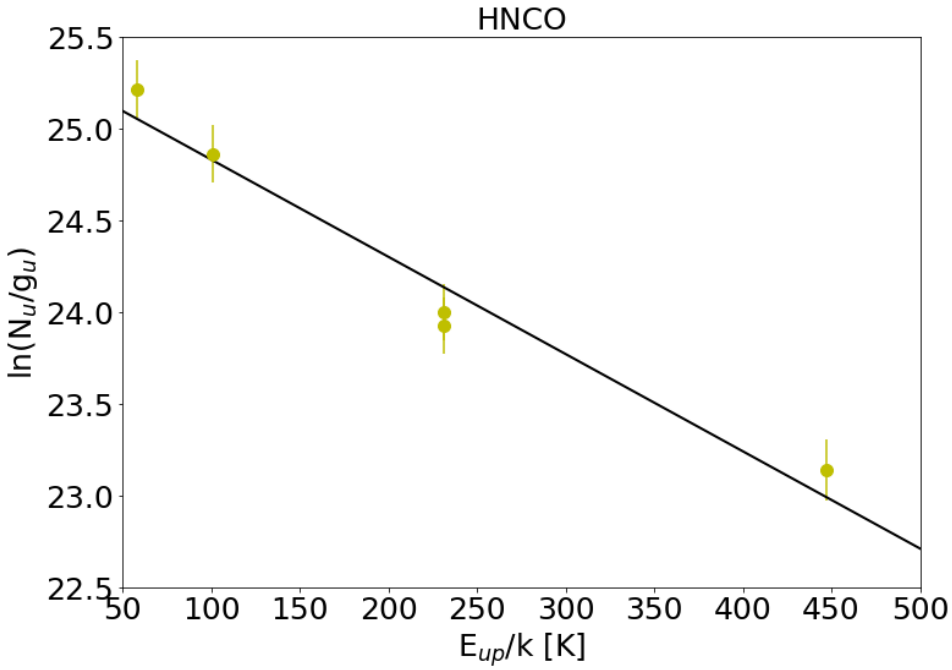


Figure 3.7: The excitation diagram for HNCO.

**Formaldehyde**

Formaldehyde is the simplest aldehyde and an abundant interstellar molecule which is suggested to be the major constituent of cometary ices. It is also believed to be the primary precursor for the prebiotic synthesis of glycine, other amino acids and in general most of the complex organic material in the interstellar medium (Gargaud et al., 2015). It is formed via hydrogenation of CO in ice, as the gas phase reaction of formaldehyde is too inefficient to produce the observed formaldehyde abundances (Gargaud et al., 2015). $H_2CO$ was first detected in the interstellar medium in 1970 by Zuckerman et al. (1970) and has since been detected in many different regions.
Within the data set 3 formaldehyde ($H_2CO$) lines were found. The emission lines are some of the strongest transitions within the spectra. One of the transitions presented itself as an absorption line, indicating that self absorption took place, leading to the line being optically thick. Also 2 doubly deuterated formaldehyde transitions were found. With these an estimation of the D/H ratio for the source can be made. For the purpose of calculating the D/H ratio as well as an excitation diagram the self absorbed emission was assumed as being optically thin and fitted accordingly.

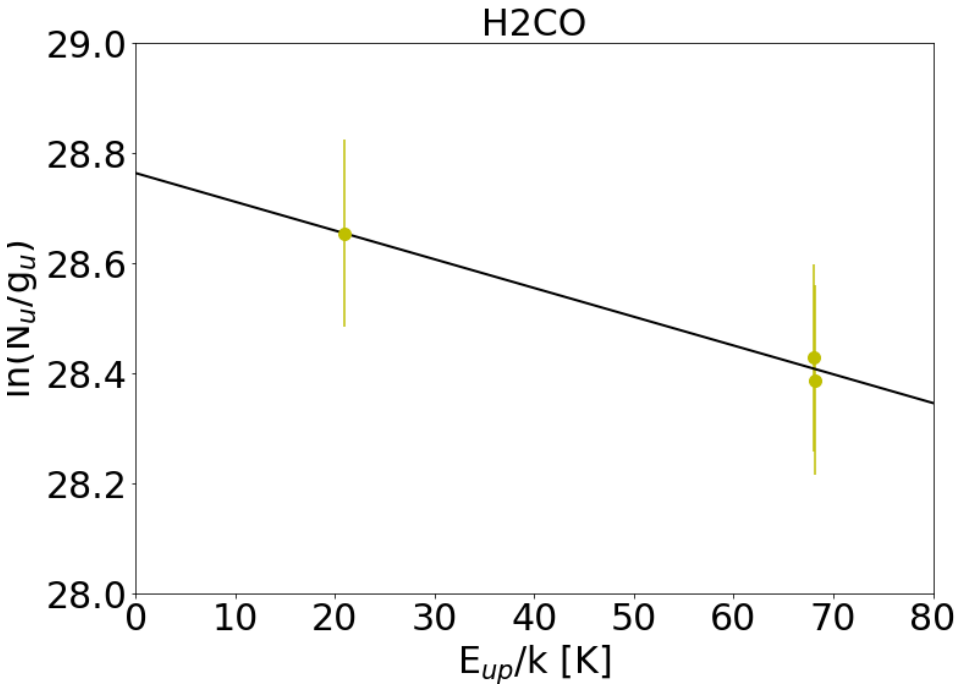


Figure 3.8: Excitation diagram for $H_2CO$.

**Acetone**

Acetone ($CH_3COCH_3$) consists of two methyl groups ($CH_3$) attached to one CO group element. These two methyl groups are two identical internal rotors and interact with each other. This leads to an E- or A- symmetry state for each of the two methyl groups; in combination with the rigid-body rotation of the molecule, this gives four possible components corresponding to the product of these symmetry states (Kwok, 2012).
In the excitation diagram it clearly shows that the linear fit strongly depends on the 218.63 GHz ($E_{up}$ = 66 K) transition. From the identified transitions one is blended and two are below the noise.

**Cyanamide**

Cyanamide ($NH_2CN$) is a nearly prolate symmetric rotor, where the amine group ($NH_2$) is attached to CN, making it also a non-planar molecule (Kwok, 2012). Its first detection in 1975 towards Sgr B2 was conducted by Turner et al. (1975).
The excitation diagram shows a nice linear fit with a relatively small scatter of the transitions and no blended transitions.

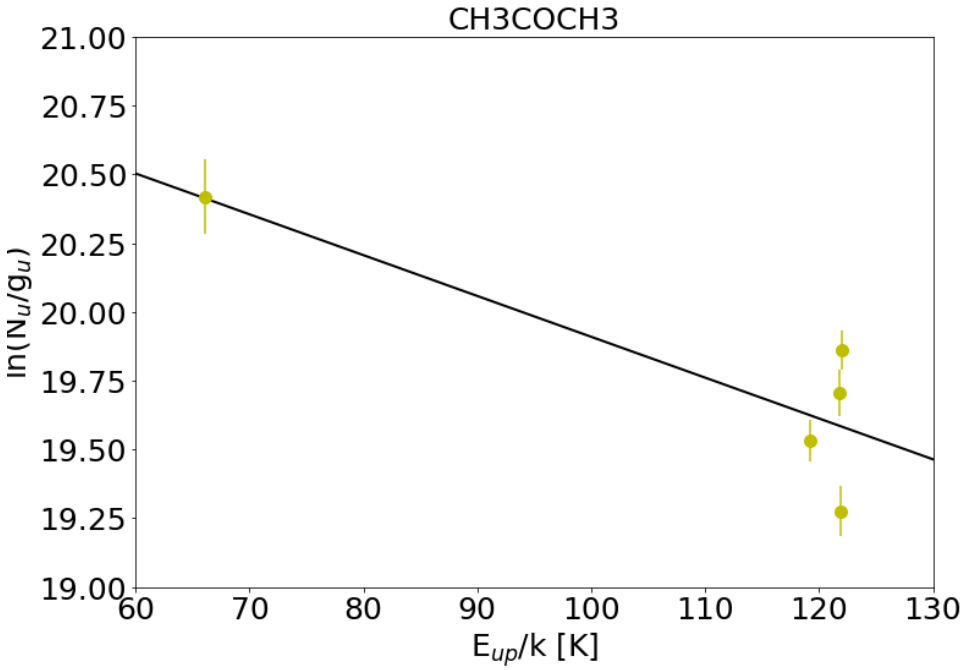


Figure 3.9: The excitation diagram for $CH_3COCH_3$.

**Cyclopropenylidene**

Cyclopropenylidene (c-$C_3H_2$) is the most abundant ring molecule in interstellar and circumstellar environments and has been observed in regions such as diffuse gas, cold dark clouds, giant molecular clouds, photodissociation regions, circumstellar envelopes, and planetary nebulae (Spezzano et al., 2013). The first detection of this molecule was in 1985 by Thaddeus et al. (1985), where previously unidentified astronomical lines could be assigned to $C_3H_2$.
The excitation diagrams shows a nice fit to the transitions, indicating that the used assumption of LTE and optically thin transitions can be used for this species.

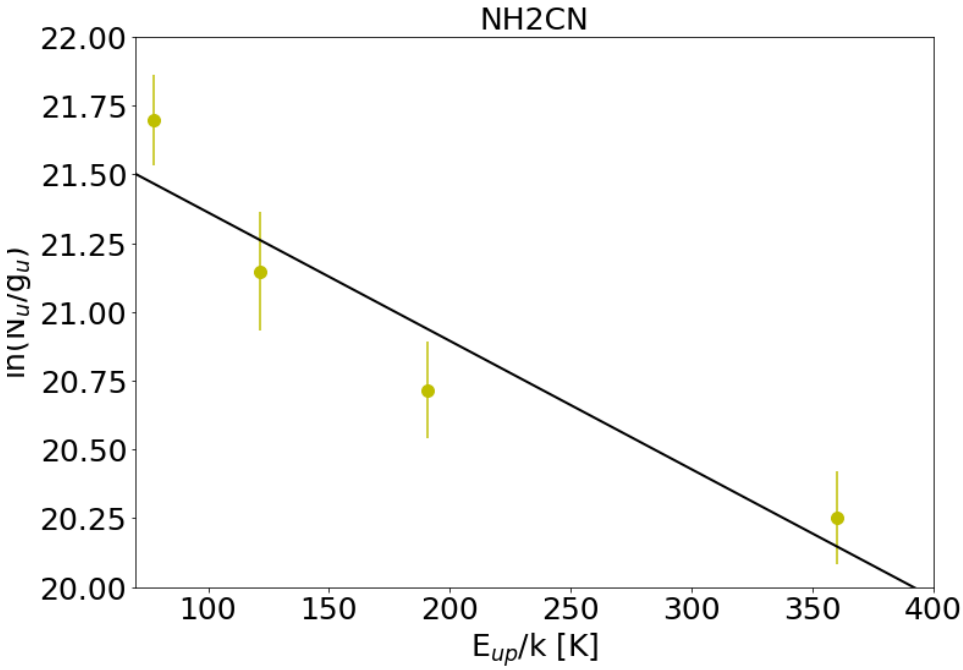


Figure 3.10: The excitation diagram for $NH_2CN$.

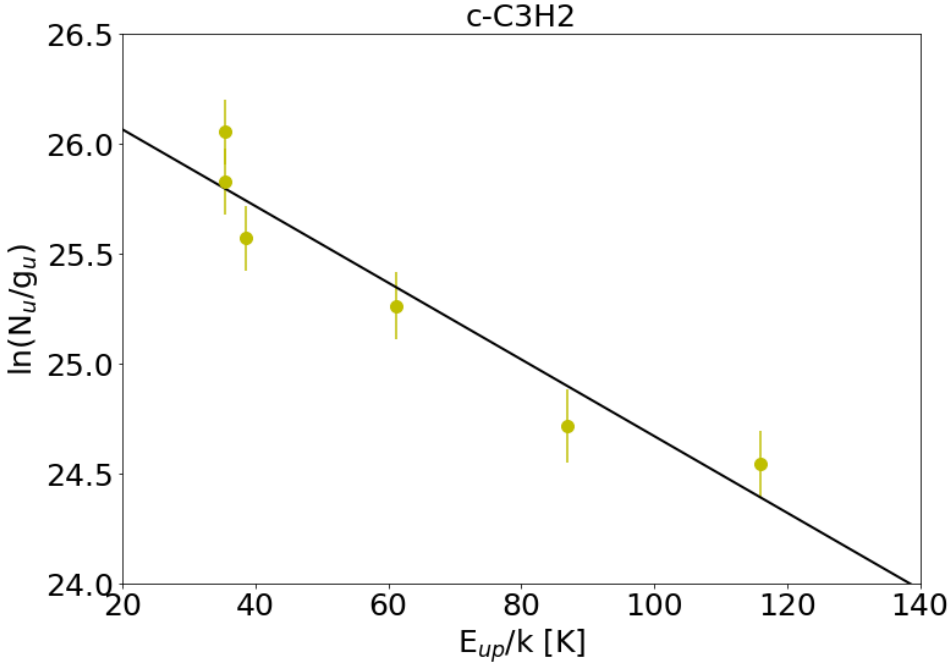


Figure 3.11: The excitation diagram for c-$C_3H_2$.

## 3.3 Synthetic spectra

In section 2.5 the usage of the synthetic spectra for a better line identification was explained. Here these synthetic spectra in comparison to the observed spectra are presented for the whole spectral range of 217.56 - 219.93 GHz and 230.28 - 232.18 GHz. The synthetic spectra were computed for the species with an excitation diagram calculation listed in table 3.1. The transitions of these 10 species as well as the other identified species are labeled within the spectra.

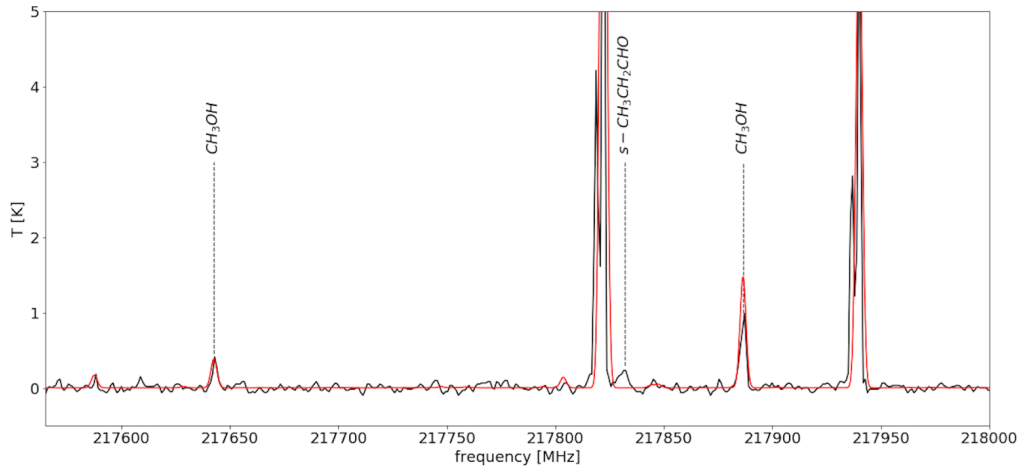


Figure 3.12: The observed spectra with the synthetic spectra for different prominent species.

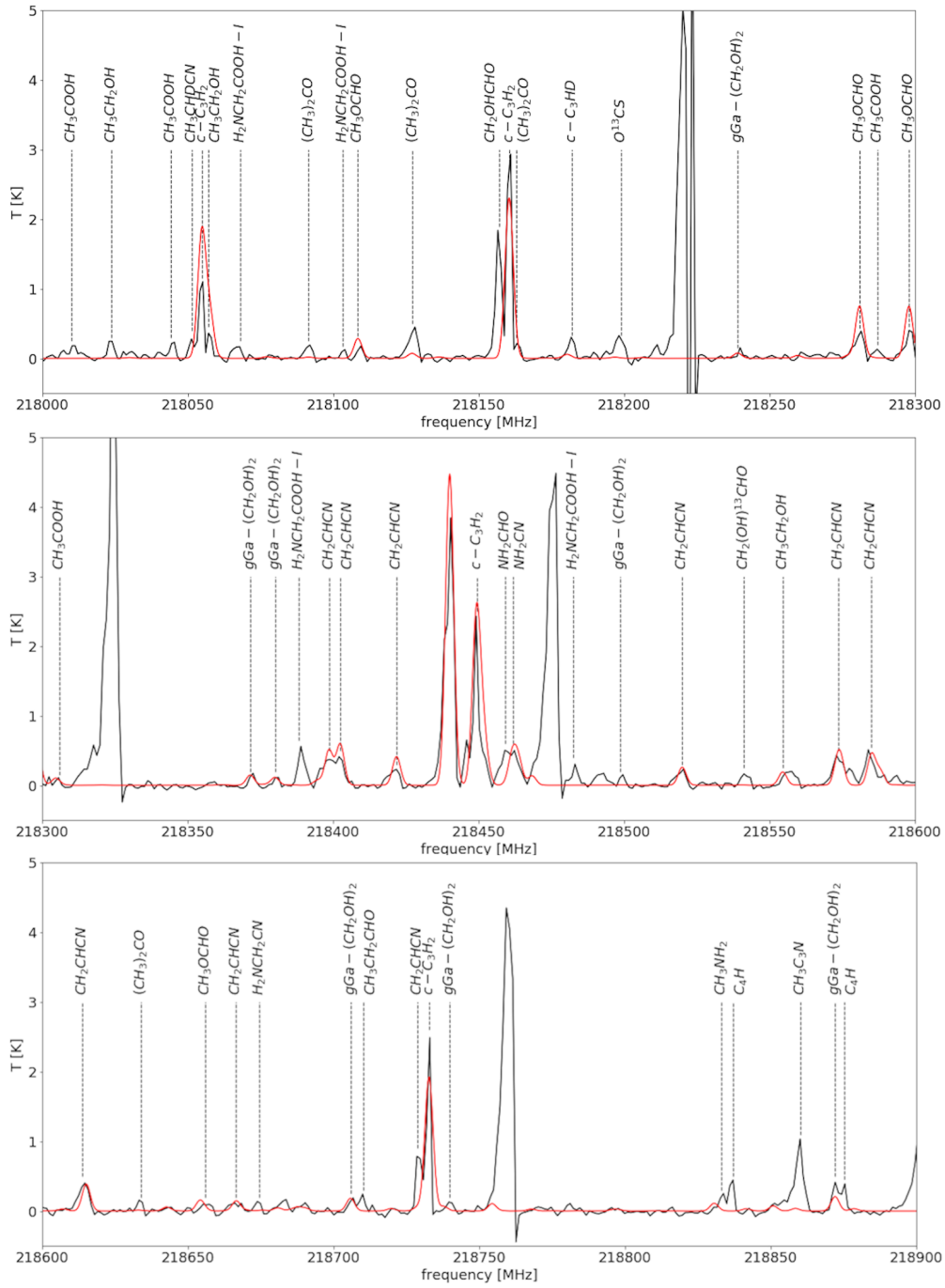


Figure 3.13: continued

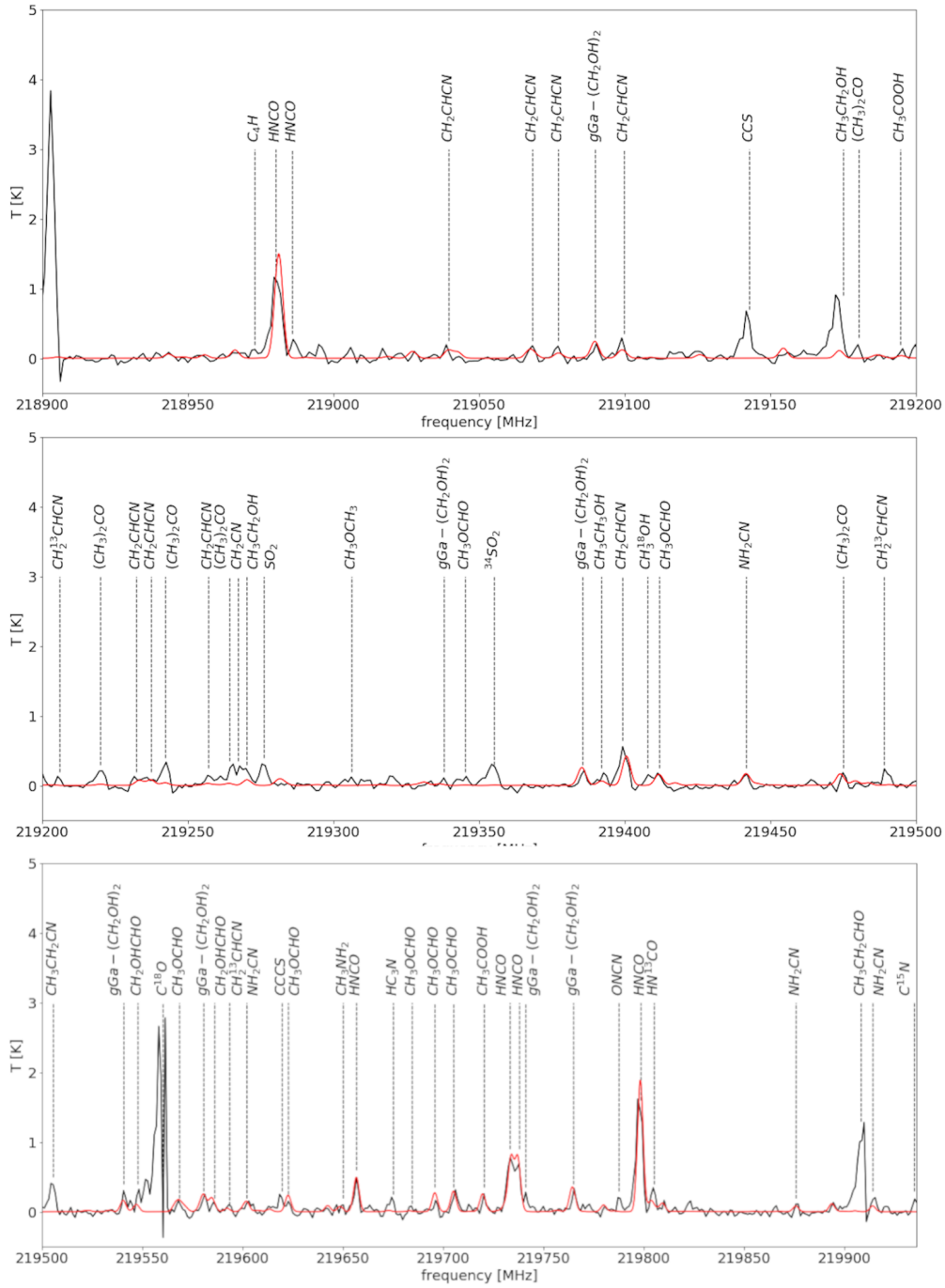


Figure 3.14: continued

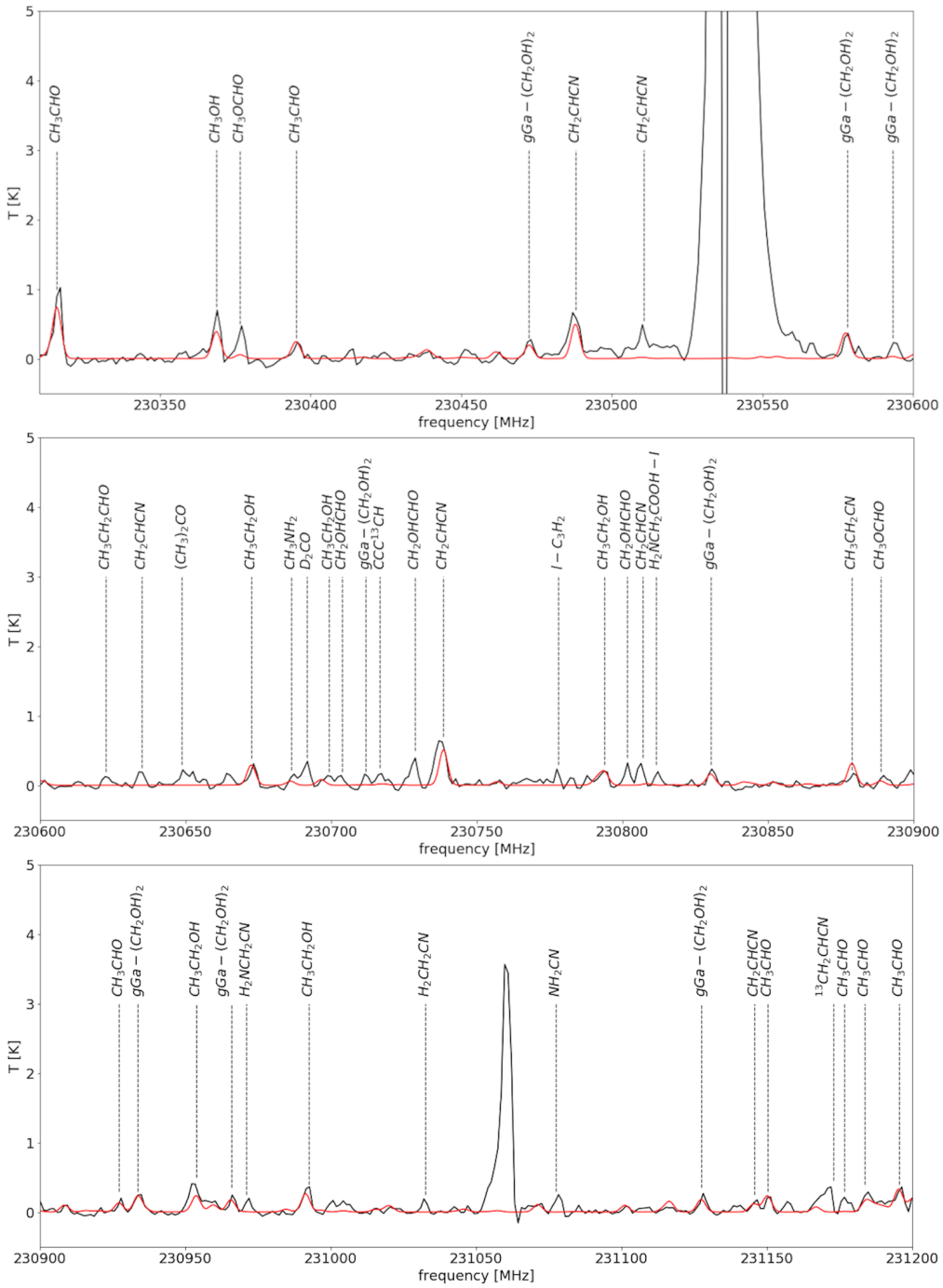


Figure 3.15: continued

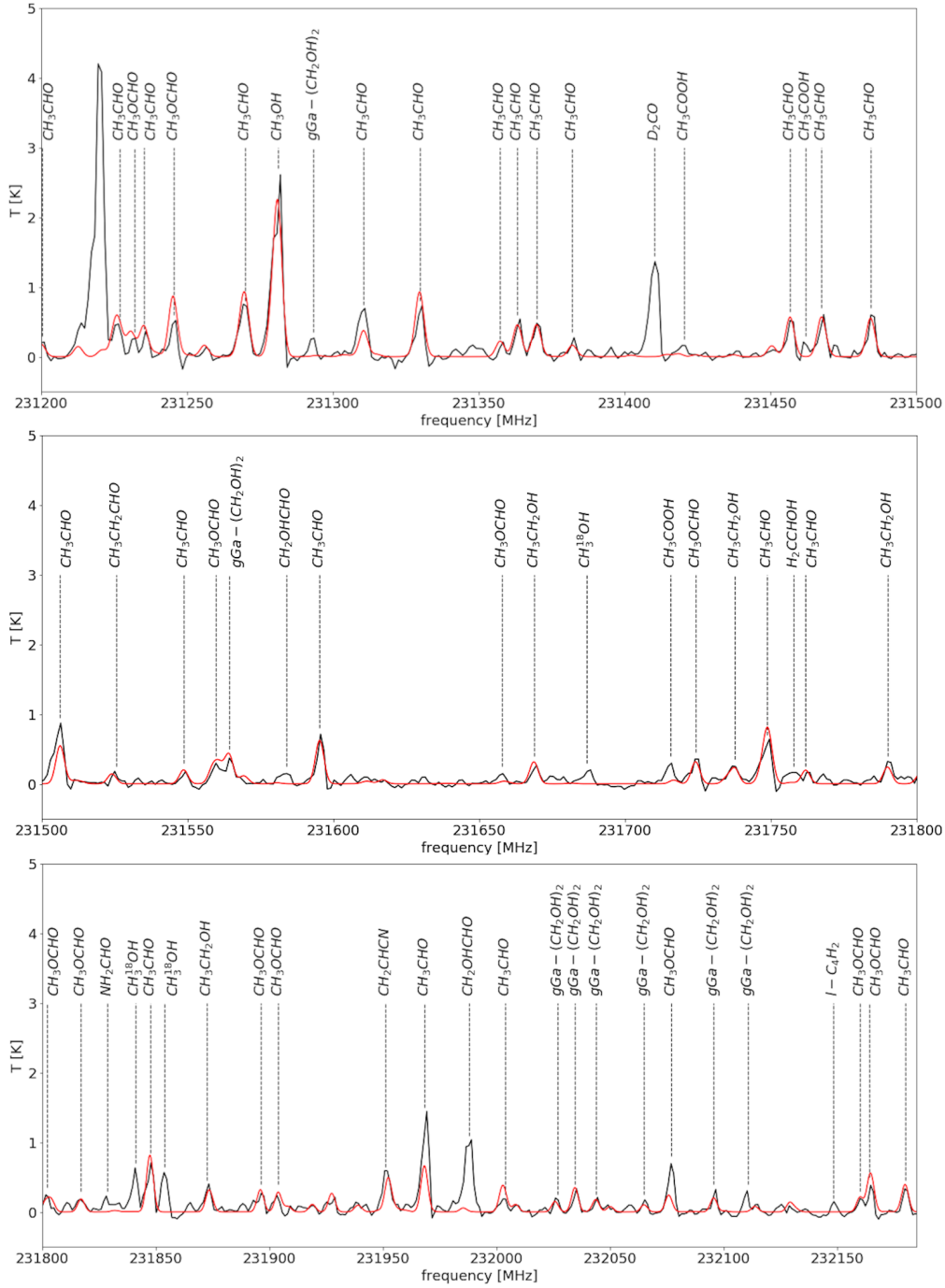


Figure 3.16: continued

## 3.4 Abundances

The calculated column densities shown in tables 3.1 and 3.2 of each species are compared to the one of $CH_3OH$, as it is the first COM to form on the grains' surface, to get abundance ratios for further comparison with other hot corinos.
Isotopologue detections for formaldehyde are made, namely doubly deuterated formaldehyde. For the calculation of the column density of the non-deuterated form $H_2CO$, we used the excitation diagram calculation explained in section 2.4. Three transitions were detected, with the 218.22 GHz transition being self-absorbed, which could be due to colder material in the foreground. We assumed the self-absorbed transition to be optically thin for calculation purposes and fitted it with a simple Gaussian. The calculated values of $4.6 \pm 0.2 \cdot 10^{15}$ cm$^{-3}$ and $191.5 \pm 27.5$ K coincide with the values from the fitted synthetic spectra to observed spectra predictions of $6 \cdot 10^{15}$ cm$^{-3}$ and 200 K. For the calculation of the doubly deuterated formaldehyde we used the excitation temperature of the non-deuterated formaldehyde, as it fits well to the proposed 200 K excitation temperature for the hot molecular species group, as explained in section 4.1. There are only two detections of $D_2CO$ and as a result the column density was calculated for each transition using equation 2.7, leading to two values. For the further calculation of the D/H ratio only the column density of the 231.41 GHz transition is used, as it is a very strong and clear line as compared to the 230.69 GHz transition and also coincides with the synthetic spectra prediction.
The transitions for $H_2CO$ and $D_2CO$ have to have the same symmetry state to be used for the column density calculation explained in section 2.4. The $H_2CO$ transitions all show a para form as seen in table 5, meaning an anti-parallel nuclear spin between the two H-atoms of the molecule. The doubly deuterated formaldehyde transitions show an ortho form (parallel spin). For formaldehyde the para form is the lowest transitional state as for the deuterated species the opposite is the case with the ortho form being the lowest transitional state (Bergman et al., 2011). It therefore follows that the transitions for formaldehyde and its isotopologue reside in the lower energy states and the D/H ratio of 5.6% could be calculated.

# Chapter 4

# Discussion

## 4.1 Excitation temperatures

The emission of a Class 0 protostellar object is expected to show an onion-like structure, with higher temperatures in the inner regions and lower temperatures in the more extended regions (Jørgensen et al., 2002). In the case of IRAS 16293-2422 A the hottest species with temperatures of 135-180 K seem to be located closer to the central source compared to species with lower excitation temperatures, the same was found for IRAS 16293-2422 B, where the lower excitation temperature species belonged to more extended regions of the hot corino (Manigand et al., 2020).

A first distinction into two groups was found by Bisschop et al. (2007), where detected species in seven high-mass YSOs showing hot core chemistry traced either hot gas ($T_{ex}$ > 100 K) or cold gas ($T_{ex}$ < 100 K). In the study by Jørgensen et al. (2018) the hot corino IRAS 16293-2422 B shows such a distinction into two components with temperature ranges of 250-300 K and 100-150 K. An explanation for these two groups could be found within the different binding energies and sublimation temperatures of the molecular species, meaning that hotter species sublimate at higher temperatures and having higher binding energies and vice versa. This approach was proposed in the three-phase chemical model of Garrod (2013). Jørgensen et al. (2018) further proposes that these different temperatures may be a result of rapid infall in the dense innermost regions of the envelope and may reflect where those species originally sublimated.

The analysis of SMM1a shows a similar outcome, with varying excitation temperatures between the different species. These temperatures could be divided in a hot group with temperatures ranging between 100-230 K and a cold group with temperatures of ~70 K. The former group includes $CH_3CH_2OH$, $CH_3CHO$,

$CH_3OCHO$, $C_2H_3CN$, HNCO, $NH_2CN$ and $CH_3OH$ with binding energies of 4500−10200 K and the latter $CH_3COCH_3$ and c-$C_3H_2$ with binding energies of 3300−3500 K. The molecules for both groups agree with the distinctions made by Jørgensen et al. (2018), except for $CH_3OCHO$, where the excitation temperature of 74.9 K and the binding energy of 5200 K do not fit in this categorization. This could be due to the strong dependence of the excitation diagram fit on three transitions with lower upper energy levels as seen in figure 3.2. In general the excitation temperatures coincide within the errors with the calculated temperatures in these studies.

## 4.2 Column densities

The calculated column densities for SMM1a and SMM1b are shown in tables 3.1 and 3.2. To put them into context their relative abundance to $CH_3OH$ is calculated as explained in section 2.4 and 3.4. These relative abundances can now be compared to other sources.

### 4.2.1 Comparison to other hot corinos

The ALMA-PILS survey conducted during the last years (Jørgensen et al. (2016), Jørgensen et al. (2018), Manigand et al. (2019), Manigand et al. (2020), Lykke et al. (2017)) studied the protostar IRAS 16293-2422 A in detail and provided comparative values. Other known hot corinos like HH212 were studied in this context by Lee et al. (2019), NGC 1333 IRAS 4A1 and 4A2 by Sahu et al. (2019) and various low mass protostars, including sources from the Perseus cloud (B1-bS, B1-c) and the Serpens cloud (S68N) by Gelder et al. (2020). We compared these sources to our data, which can be seen in figure 4.1. The deviations between the sources are of a factor of a few, but show for all species an overabundance relative to $CH_3OH$ for the SMM1a source. The column densities of SMM1a themselves are comparable to those from other studies, except for $CH_3OH$, where the column density of $3.2 \cdot 10^{16}$ cm$^{-3}$ is underestimated as compared to these studies. These column densities are for example $1.3 \cdot 10^{19}$ cm$^{-3}$ for IRAS 16293-2422 A (Manigand et al., 2020), $6.1 \cdot 10^{17}$ cm$^{-3}$ for HH212 (Lee et al., 2019), $1.0 \cdot 10^{19}$ cm$^{-3}$ for IRAS 16293-2422 B (Jørgensen et al., 2018) and $1.4 \cdot 10^{18}$ cm$^{-3}$ for S68N (Gelder et al., 2020), to name a few. This difference in the column density of the reference species for the abundances leads to the abundances of SMM1a and SMM1b to be overestimated. Apart from that the abundance ratios are still quite similar,

although these sources are located in different star forming regions and show different properties. This could indicate that for these sources (hot corinos) a similar formation scheme could be applied (Gelder et al., 2020).

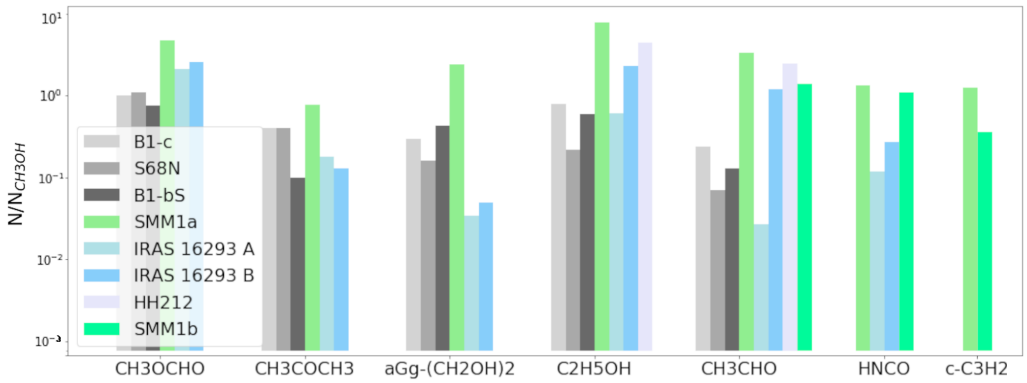


Figure 4.1: Comparison of the abundances relative to $CH_3OH$ for SMM1a and SMM1b data to other hot corinos. Values for B1-c, S68N and B1-bS are taken from Gelder et al. (2020) and for HH212 from Lee et al. (2019). The abundance ratios for IRAS 16293A are from Manigand et al. (2020) and for IRAS 16293B from Jørgensen et al. (2018).

### 4.2.2 Comparison of SMM1a and SMM1b

SMM1 is a multiple system harbouring the protostellar binary SMM1a and SMM1b. These two sources are expected to be binaries themselves, which leads to a potentially unstable system, meaning that in the further evolution it will eject an object. SMM1a is the stronger source in the binary and is entangled with SMM1b, as seen in velocity channel maps shown in the appendix figures 5.1 - 5.3 of some of the strongest transitions, where the extend and distribution of the species within the sources and between them can be seen. The different transitions of each source overlap in species as shown in the appendix line table 5, but in general the transitions flux is lower for SMM1b. The variety and number of transitions and species is also lower in SMM1b, where only a fourth of the number of transitions of SMM1a is detected. The calculated excitation temperatures and column densities of 5 species show similar values to SMM1a. The higher errors within the calculation of $CH_3CHO$ and $CH_3OCHO$ can be attributed to the lack of transitions compared to SMM1a. The comparison of the relative abundances shown in figure 4.1 for $CH_3CHO$, HNCO and c-$C_3H_2$ also shows similar values. This similarity between the components of a binary is also found in the study of Manigand et al. (2020), where IRAS 16293-2422 A and B are analysed. A is in this case

the brighter source and B the one lacking COMs. They suggest that the B source started collapsing later than A, due to fragmentation of the parent cloud. Another example for a binary with differing abundances is NGC 1333 IRAS 4A. In the study from López-Sepulcre et al. (2017) they suggest different scenarios for the lack of COMs towards the A1 source as compared to A2, which is a typical hot corino. They suggest that A1 might either contain a hot corino, but is heavily obscured by a very compact disk or hosts no hot corino and is not yet in the collapse phase.

## 4.3 Deuterated species

The deuteration fraction of different species is often used to understand the water delivery to Earth through comparing the D/H ratios of different bodies, but another interesting factor is at what point deuterated water is formed and the processing before it ended up in the protoplanetary disk. As the formation of deuterated water is inefficient within this environment, studying this formation in earlier stages, like the pre-stellar phase gets important (Jørgensen et al., 2020). We calculated the deuteration fraction towards SMM1a for formaldehyde and its doubly deuterated form as explained in section 2.4 and 3.4. The D/H ratio is 5.6% and comparable to other sources, as measurements for the D/H ratio towards IRAS 16293-2422 from Loinard et al. (2000) with single dish observations show a $D_2CO/H_2CO$ ratio of 5-6%, also showing absorption signatures for $H_2CO$. Observations with a higher angular resolution towards this source show D/H ratio measurements for this isotopologue of 8% (Persson et al., 2018) and of $2.0 \pm 0.4 \cdot 10^{-1}$ (Manigand et al., 2020). This high deuterium fractination is several orders of magnitude higher than the cosmic D/H ratio ($2 \cdot 10^{-5}$) and common for low-mass protostars. It is believed that the freeze-out of CO on grains, low temperatures and a drop in the ortho-to-para ratio of $H_2$ causes the deuteration to be more efficient (Jørgensen et al., 2020; Bergman et al., 2011). The D/H ratio is also higher compared to the ones of high-mass protostars and in case of IRAS 16293-2422 B the COMs do not show variations in their D/H ratios, which leads to the conclusion of a homogeneous time of formation during the cold phase, where the exchange reactions in the later warm gas phase play a smaller role according to Jørgensen et al. (2020).

# Chapter 5

# Conclusions

In this master's thesis observations from two ALMA projects were used to analyse the protostellar binary SMM1/FIRS1 with its two sources SMM1a and SMM1b in the context of their COM and the excitation temperatures and column densities of these COMs. The results can be summarized as follows:

- The hot corino source SMM1a shows various COM transitions, with 10 of them having enough unblended transitions to conduct an excitation diagram analysis. The resulting column densities of the species are comparable to other hot corinos, except for $CH_3OH$, where the column densities are 1-3 orders of magnitude lower than in similar sources, which leads to an overestimated relative abundance of other COMs in the comparison to those other sources, but the values are still quite similar. This could imply that for hot corinos a similar formation scheme is present, regardless of formation environment and source properties.

- The calculated temperatures for the COMs towards SMM1a also coincide with other sources and seem to trace two temperature regimes, a hot group tracing the more compact inner regions and a cold group tracing the more extended regions of the source. The only exception is $CH_3OCHO$, where the temperature would indicate a cold group member, but the binding energy of a hot species.

- The analysis of the second binary component SMM1b shows less variation and quantity of transitions as compared to SMM1a. The relative abundances and excitation temperatures of four of the analysed COMs are similar to those of SMM1a. The lack of COMs towards SMM1b could be the result of the source starting to collapse later than SMM1a, or it being more obscured by a very compact disk.

- The D/H ratio of doubly deuterated formaldehyde of 5.6% towards SMM1a is higher than the cosmic D/H ratio, as also found for other hot corinos like IRAS 16293-2422. Further observations are needed for a comparison of multiply deuterated to singly deuterated species to confirm a possible higher D/H ratio for multiply deuterated species, which has been detected for other deuterated species in hot corinos.

# Appendix

## Velocity channel maps

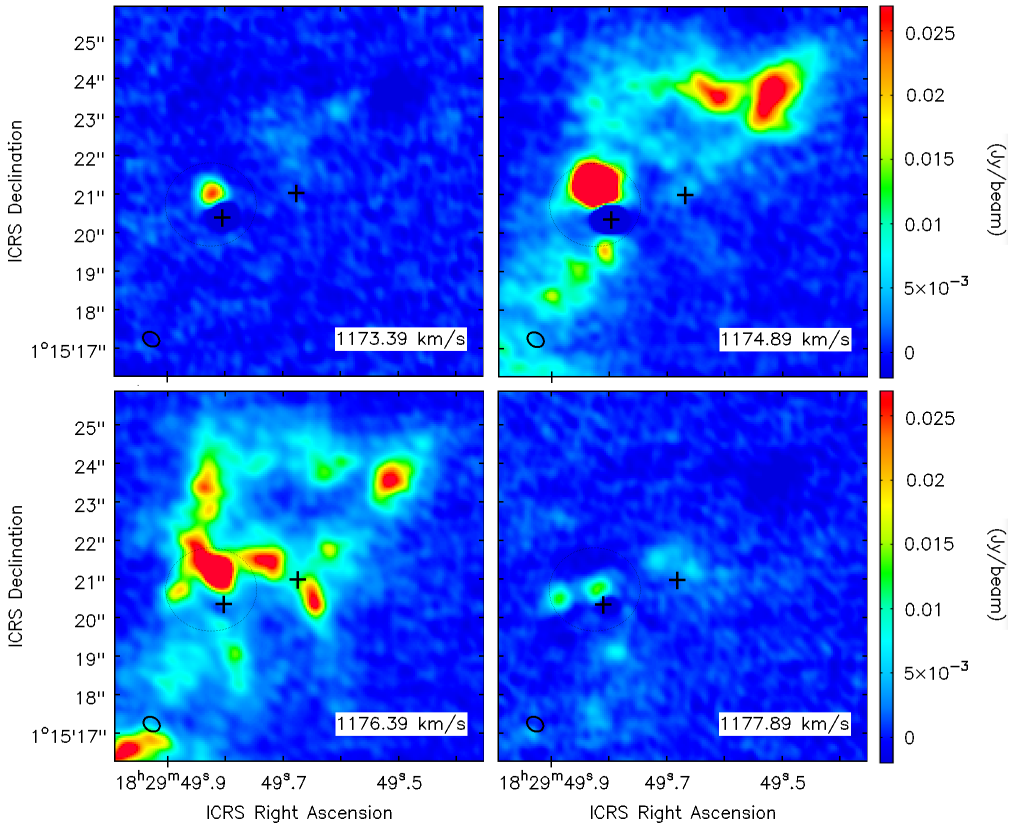


Figure 5.1: Velocity channel map of the c-$C_3H_2$ transition at 218.160 GHz. The right cross marks the position of SMM1b and the left one of SMM1a.

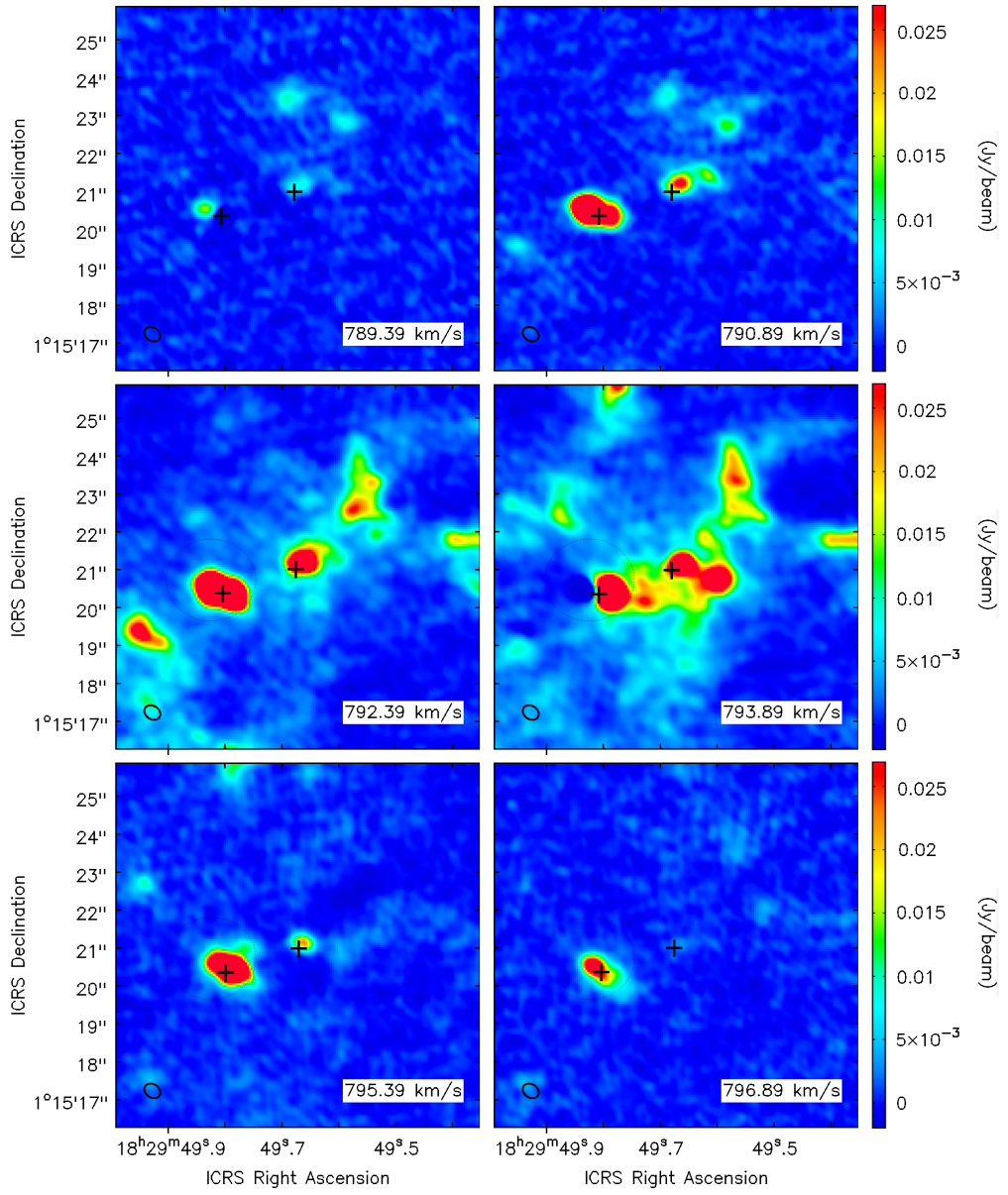


Figure 5.2: Velocity channel map of the $CH_3OH$ transition at 218.440 GHz. The right cross marks the position of SMM1b and the left one of SMM1a.

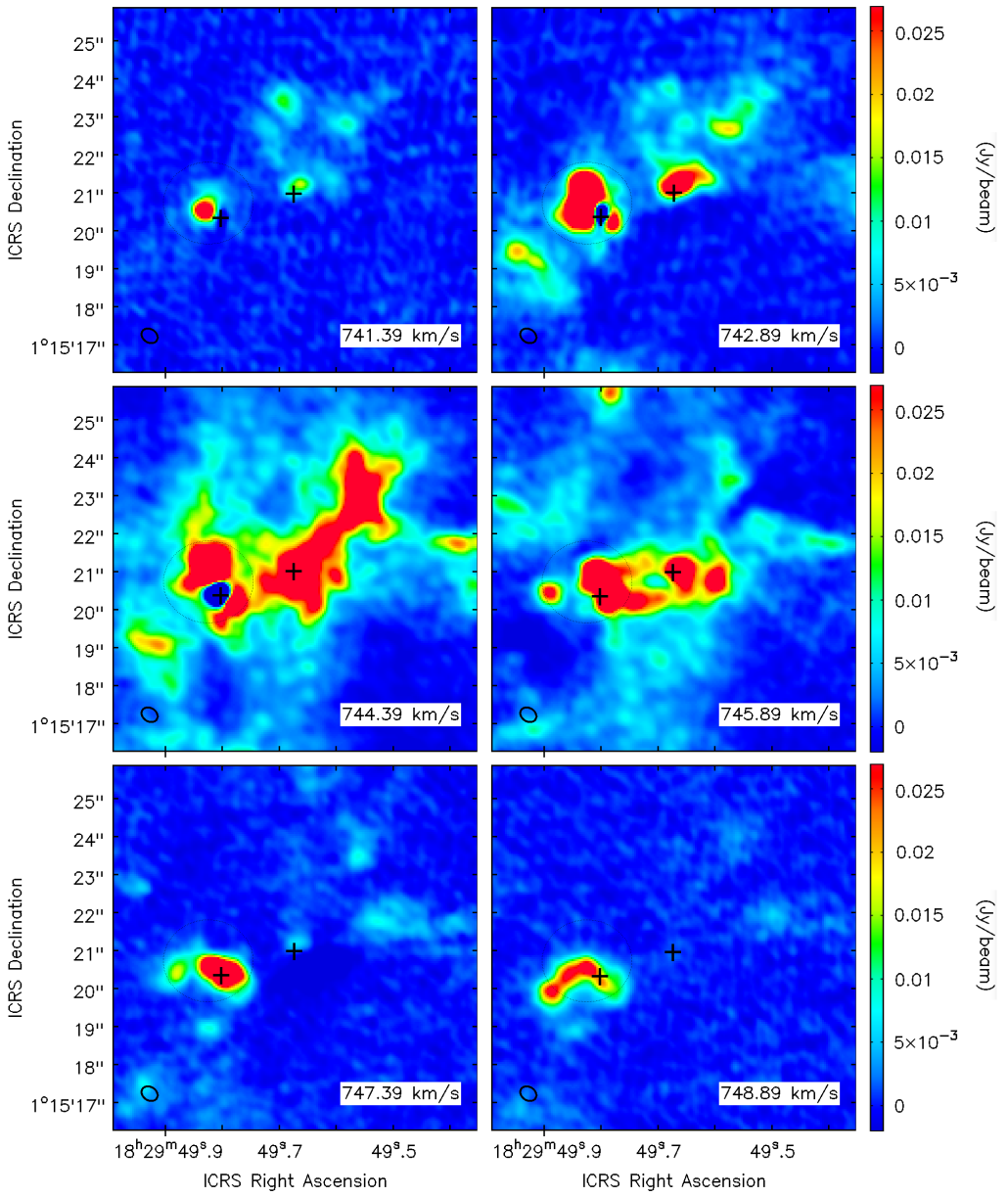


Figure 5.3: Velocity channel map of the $H_2CO$ transition at 218.475 GHz. The right cross marks the position of SMM1b and the left one of SMM1a.

## Lines per species used for calculation and fitting

| Species | Transition<br>J ($k_a$, $k_c$) - J ($k_a$, $k_c$) | Frequency<br>MHz | $E_{up}$<br>K | $G_{up}$ | $A_{ij}$<br>$s^{-1}$ | Flux<br>K · km/s | Flux (SMM1b)<br>K · km/s |
|---|---|---|---|---|---|---|---|
| HNCO | 10 (1,10) - 9 (9,1), F=9-9 | 218980.25 | 101.08 | 19 | $1.6 \cdot 10^{-6}$ | 6.26 | 5.32 |
| | 10 (3,8) - 9 (3,7), F=10-9 | 219656.74 | 447.46 | 21 | $1.4 \cdot 10^{-4}$ | 2.06 | 1.35 |
| | 10 (2,9) - 9 (9,2), F=8-9 | 219733.12 | 231.11 | 19 | $1.6 \cdot 10^{-6}$ | 4.78 | 4.05 |
| | 10 (2,8) - 9 (9,2), F=7-8 | 219737.19 | 231.11 | 19 | $1.4 \cdot 10^{-4}$ | 4.91 | 4.07 |
| | 10 (0,10) - 11 (9,0), F=9-10 | 219798.32 | 58.02 | 23 | $1.5 \cdot 10^{-4}$ | 9.05 | 6.78 |
| CH3OH | 15 (6,1) - 16 (5,1) | 217642.68 | 745.61 | 31 | $1.9 \cdot 10^{-5}$ | 1.38 | 1.72 |
| | 20 (1,0) - 20 (0,0) | 217886.50 | 508.38 | 41 | $3.4 \cdot 10^{-5}$ | 4.16 | 3.64 |
| | 4 (2,0) - 3(1,0) | 218440.06 | 45.46 | 9 | $4.7 \cdot 10^{-5}$ | 19.83 | 22.97 |
| | 22 (4,0) - 21 (5,0) | 230368.76 | 682.75 | 45 | $2.1 \cdot 10^{-5}$ | 2.83 | 4.68 |
| | 10 (2,0) - 9 (3,0) | 231281.11 | 165.35 | 21 | $1.8 \cdot 10^{-5}$ | 12.71 | 15.61 |
| c-$C_3H_2$ | 6 (1,6) - 5 (0,5) | 217822.15 | 38.61 | 39 | $5.9 \cdot 10^{-4}$ | 21.27 | 9.71 |
| | 5 (1,4) - 4 (2,3) | 217940.05 | 35.42 | 33 | $4.4 \cdot 10^{-4}$ | 16.32 | 5.51 |
| | 9 (3,6) - 9 (2,7) | 218054.78 | 115.91 | 57 | $2.1 \cdot 10^{-4}$ | 2.96 | 1.29 |
| | 5 (2,4) - 4 (1,3) | 218160.44 | 35.418 | 11 | $4.4 \cdot 10^{-4}$ | 8.69 | 5.01 |
| | 8 (3,6) - 8 (2,7) | 218449.44 | 86.94 | 51 | $1.6 \cdot 10^{-4}$ | 6.52 | 3.62 |
| | 7 (1,6) - 7 (0,7) | 218732.73 | 61.17 | 45 | $9.8 \cdot 10^{-5}$ | 5.93 | 3.78 |
| $NH_2CN$ | 11 (1,11) - 10 (1,10), v=0 | 218461.80 | 77.41 | 69 | $1.1 \cdot 10^{-4}$ | 2.12 | |
| | 11 (2,10) - 10 (2,9), v=1 | 219441.60 | 191.02 | 69 | $1.0 \cdot 10^{-3}$ | 0.74 | |
| | 11 (4,7) - 10 (4,6), v=1 | 219602.12 | 360.33 | 69 | $9.3 \cdot 10^{-4}$ | 0.86 | |
| | 11 (2,10) - 10 (2,9), v=0 | 219875.83 | 121.29 | 23 | $1.1 \cdot 10^{-3}$ | 0.40 | |

| | | | | | | | |
|---|---|---|---|---|---|---|---|
| $CH_3COCH_3$ | 20 (2,18) - 19 (3,17), EA | 218091.45 | 119.18 | 164 | $4.3 \cdot 10^{-4}$ | 0.93 | |
| | 12 (9,4) - 11 (8,3), EE | 218633.85 | 66.04 | 400 | $1.8 \cdot 10^{-4}$ | 0.56 | |
| | 21 (1,20) - 20(2,19), EA | 219219.97 | 121.99 | 172 | $4.7 \cdot 10^{-4}$ | 1.46 | |
| | 21 (1,20) - 20 (2,19), EE | 219242.14 | 121.91 | 688 | $3.9 \cdot 10^{-5}$ | 1.63 | |
| | 21 (1,20) - 20 (2,19), AA | 219264.28 | 121.83 | 258 | $4.7 \cdot 10^{-4}$ | 1.25 | |
| $CH_3OCHO$ | 17 (4,13) - 16 (4,12), E, v=1 | 218108.44 | 289.68 | 70 | $1.5 \cdot 10^{-4}$ | 0.60 | |
| | 18 (10,8) - 17 (10,7), E, v=1 | 219411.70 | 354.93 | 74 | $1.1 \cdot 10^{-4}$ | 0.76 | |
| | 18 (12,7) - 17 (12,6), A, v=1 | 219622.69 | 383.96 | 74 | $8.9 \cdot 10^{-5}$ | 0.73 | |
| | 18 (11,8) - 17 (11,7), A, v=1 | 219695.83 | 368.60 | 74 | $1.0 \cdot 10^{-4}$ | 0.58 | |
| | 18 (4,15) - 17 (4,14), A, v=1 | 219705.13 | 298.98 | 74 | $1.5 \cdot 10^{-4}$ | 1.31 | |
| | 22( 9,14)-22( 8,15), E, v=0 | 230315.80 | 203.35 | 90 | $1.5 \cdot 10^{-5}$ | | 4.26 |
| | 22 (9,14) - 22 (8,15), A, v=0 | 230376.59 | 203.36 | 90 | $1.6 \cdot 10^{-5}$ | 1.83 | 2.69 |
| | 18 (4,14) - 17 (4,13), A, v=1 | 230878.81 | 301.04 | 74 | $1.8 \cdot 10^{-4}$ | 0.86 | |
| | 19 (4,16) - 18 (4,15), A, v=1 | 231245.42 | 310.07 | 78 | $1.8 \cdot 10^{-4}$ | 2.03 | |
| | 27 (3,25) - 27 (2,26), E, v=0 | 231559.69 | 221.73 | 110 | $7.2 \cdot 10^{-6}$ | 1.59 | 2.84 |
| | 27 (3,25) - 27 (2,26), A, v=0 | 231658.06 | 221.72 | 110 | $7.2 \cdot 10^{-6}$ | 0.70 | |
| | 18 (4,14) - 17 (4,13), E, v=1 | 231724.16 | 300.80 | 74 | $1.8 \cdot 10^{-4}$ | 1.45 | 2.63 |
| | 19 (14,5) - 18 (14,4), A, v=1 | 231816.99 | 429.85 | 78 | $8.6 \cdot 10^{-5}$ | 1.15 | |
| | 19 (13,6) - 18 (13,5), A, v=1 | 231846.82 | 411.79 | 78 | $1.0 \cdot 10^{-4}$ | | 2.52 |
| | 19 (4,16) - 18 (4,15), E, v=1 | 231896.06 | 309.75 | 78 | $01.8 \cdot 10^{-4}$ | 1.01 | |
| | 19 (12,7) - 18 (12,6), A, v=1 | 231903.91 | 395.09 | 78 | $1.1 \cdot 10^{-4}$ | 1.02 | |
| | 23 (9,15) - 23 (8,16), A, v=1 | 232077.29 | 403.69 | 94 | $1.7 \cdot 10^{-5}$ | | 4.24 |

| | | | | | | | |
|---|---|---|---|---|---|---|---|
| | 19 (10,10) - 18 (10,9), A, v=1 | 232164.44 | 365.73 | 78 | $1.4 \cdot 10^{-4}$ | 1.3 | |
| $CH_3CHO$ | 12 (2,11) - 11 (2,10), E, vt=0 | 230315.79 | 81.06 | 50 | $4.0 \cdot 10^{-4}$ | 3.93 | |
| | 12 (2,11) - 11 (2,10), A, vt=1 | 230395.16 | 286.41 | 50 | $4.1 \cdot 10^{-4}$ | 1.68 | |
| | 12 (6,6) - 11 (6,5), E, vt=1 | 230927.18 | 359.37 | 50 | $3.2 \cdot 10^{-4}$ | 0.61 | |
| | 12 (8,4) - 11 (8,3), E, vt=1 | 231200.04 | 420.77 | 50 | $2.3 \cdot 10^{-4}$ | 0.65 | |
| | 12 (5,7) - 11 (5,6), E, vt=0 | 231363.28 | 128.54 | 50 | $3.5 \cdot 10^{-4}$ | 1.97 | 0.91 |
| | 12 (5,8) - 11(5,7), E, vt=0 | 231369.83 | 128.51 | 50 | $3.5 \cdot 10^{-4}$ | 2.55 | 1.97 |
| | 12 (5,8) - 11 (5,7), E, vt=1 | 231382.11 | 333.58 | 50 | $3.5 \cdot 10^{-4}$ | 0.85 | |
| | 12 (4,8) - 11 (4,9), A, vt=0 | 231456.74 | 108.35 | 50 | $3.8 \cdot 10^{-4}$ | 1.88 | 1.74 |
| | 12 (4,8) - 11 (4,7), A, vt=0 | 231467.50 | 108.35 | 50 | $3.8 \cdot 10^{-4}$ | 2.02 | 1.56 |
| | 12 (4,8) - 11 (4,7), E, vt=0 | 231484.37 | 108.29 | 50 | $3.8 \cdot 10^{-4}$ | 2.36 | 2.45 |
| | 12 (4,9) - 11 (4,8), E, vt=0 | 231506.29 | 108.25 | 50 | $3.8 \cdot 10^{-4}$ | 4.58 | 4.07 |
| | 12 (7,5) - 11 (7,4), A, vt=1 | 231548.63 | 387.01 | 50 | $2.8 \cdot 10^{-4}$ | 0.88 | |
| | 12 (3,10) - 11 (3,9), A, vt=0 | 231595.27 | 92.58 | 50 | $3.9 \cdot 10^{-4}$ | 2.57 | 2.19 |
| | 12 (3,9) - 11 (3,8), E, vt=0 | 231847.58 | 92.61 | 50 | $3.9 \cdot 10^{-4}$ | 3.41 | |
| | 12 (3,9) - 11 (3,8), A, vt=0 | 231968.38 | 92.63 | 50 | $3.9 \cdot 10^{-4}$ | 6.70 | |
| | 12 (5,7) - 11 (5,6), A, vt=1 | 232180.27 | 331.84 | 50 | $3.5 \cdot 10^{-4}$ | 1.40 | |
| aGg'$(CH_2OH)_2$ | 22 (4,19) - 21 (4,18) | 218371.49 | 132.56 | 405 | $1.9 \cdot 10^{-4}$ | 0.64 | |
| | 22 (15,7) - 21 (15,6) | 218379.98 | 234.79 | 315 | $1.4 \cdot 10^{-4}$ | 0.45 | |
| | 22 (12,10) - 21 (12,9) | 218705.81 | 195.06 | 315 | $1.8 \cdot 10^{-4}$ | 1.07 | |
| | 22 (11,11) - 21 (11,10) | 218872.11 | 183.79 | 315 | $1.9 \cdot 10^{-4}$ | 1.56 | |
| | 22 (10,13) - 21 (10,12) | 219089.72 | 173.52 | 405 | $2.0 \cdot 10^{-4}$ | 0.79 | |
| | 22 (1,21) - 21 (1,20) | 219580.67 | 122.05 | 405 | $2.6 \cdot 10^{-4}$ | 1.35 | |

| | | | | | | | |
|---|---|---|---|---|---|---|---|
| | 20 (4,16) - 19 (4,15) | 219764.93 | 113.51 | 369 | $2.5 \cdot 10^{-4}$ | 1.25 | |
| | 21 (4,17) - 20 (4,16) | 230472.53 | 124.25 | 301 | $2.8 \cdot 10^{-4}$ | 1.55 | |
| | 24 (2,22) - 23 (2,21) | 230830.32 | 149.76 | 343 | $2.8 \cdot 10^{-4}$ | 1.08 | |
| | 23 (3,20) - 22 (3,19) | 230933.68 | 143.35 | 423 | $3.2 \cdot 10^{-4}$ | 1.53 | |
| | 23 (7,16) - 22 (7,15) | 231127.40 | 160.22 | 423 | $2.7 \cdot 10^{-4}$ | 0.92 | |
| | 24 (0,24) - 23 (0,23) | 231564.32 | 136.79 | 441 | $3.0 \cdot 10^{-4}$ | 1.38 | |
| | 22 (13,9) - 21 (13,8) | 232043.88 | 207.64 | 405 | $1.9 \cdot 10^{-4}$ | 0.76 | |
| | 22 (12,10) - 21 (12,9) | 232095.74 | 195.38 | 405 | $2.1 \cdot 10^{-4}$ | 1.15 | |
| $C_2H_5OH$ | 9 (3,7) - 9 (2,7), vt=1-0 | 219270.29 | 110.04 | 19 | $3.5 \cdot 10^{-5}$ | 1.47 | |
| | 14 (2,12) - 13 (1,12), vt=0-1 | 219392.06 | 150.54 | 29 | $2.2 \cdot 10^{-5}$ | 0.68 | |
| | 13 (2,11) - 12 (2,10), vt=0-0 | 230672.55 | 138.62 | 27 | $1.1 \cdot 10^{-4}$ | 1.22 | |
| | 6 (5,2) - 5 (4,2) , vt=0-1 | 230793.86 | 104.80 | 13 | $6.1 \cdot 10^{-5}$ | 1.34 | |
| | 16 (5,11) - 16 (4,12), trans | 230953.78 | 145.78 | 33 | $7.1 \cdot 10^{-5}$ | 2.65 | |
| | 20 (5,16) - 20 (4,17), trans | 231560.90 | 208.21 | 41 | $7.4 \cdot 10^{-5}$ | 1.42 | |
| | 14 (1,14) - 13 (1,13), vt=0-0 | 231668.73 | 141.90 | 29 | $1.1 \cdot 10^{-4}$ | 1.12 | |
| | 19 (5,15) - 19 (4,16), trans | 231737.61 | 191.33 | 39 | $7.3 \cdot 10^{-5}$ | 2.49 | |
| | 22 (5,18) - 22 (4,19), trans | 231790.00 | 244.54 | 45 | $7.4 \cdot 10^{-5}$ | 1.48 | |
| $C_2H_3CN$ | 23 (8,16) - 22 (8,15), A, F=23-23 | 218420.88 | 263.81 | 47 | $1.4 \cdot 10^{-6}$ | 1.75 | |
| | 23 (10,14) - 22 (10,13), A, F=23-23 | 218519.36 | 341.06 | 47 | $1.3 \cdot 10^{-6}$ | 1.45 | |
| | 23 (4,20) - 22 (4,19), A, F=23-22 | 218573.64 | 160.39 | 47 | $8.3 \cdot 10^{-4}$ | 2.75 | |
| | 23 (4,19) - 22 (4,18), A, F=23-23 | 218613.81 | 160.40 | 47 | $1.6 \cdot 10^{-6}$ | 2.66 | |
| | 23 (6,18) - 22 (6,17), A, F=22-21, v11=1 | 219039.40 | 531.19 | 45 | $8.0 \cdot 10^{-4}$ | 0.61 | |
| | 23 (9,14) - 22 (9,13), A, F=23-22, v11=1 | 219077.03 | 626.61 | 47 | $7.3 \cdot 10^{-4}$ | 0.80 | |

| | | | | | | | |
|---|---|---|---|---|---|---|---|
| | 23 (5,18) - 22 (5,17), A, F=23-23, v11=1 | 219098.54 | 507.82 | 47 | $1.6 \cdot 10^{-6}$ | 0.94 | |
| | 23 (4,20) - 22 (4,19), A, F=23-23, v11=1 | 219232.04 | 488.71 | 47 | $1.6 \cdot 10^{-6}$ | 0.53 | |
| | 24 (1,23) - 23 (1,22), A, F=24-23 | 230487.93 | 141.25 | 49 | $1.0 \cdot 10^{-3}$ | 4.05 | |
| | 25 (0,25) - 24 (0,24), A, F=25-24, v11=1 | 231145.70 | 474.32 | 51 | $1.0 \cdot 10^{-3}$ | 0.74 | |

Table 5.1: The used transitions of each species for the excitation diagram calculations. The columns show the species name, the transition, the frequency, the upper energy level $E_{up}$, the upper state degeneracy $G_{up}$, the Einstein coefficient $A_{ij}$, the flux of the SMM1a transition and the flux of the SMM1b transition.

# Bibliography

André, P. 2011, Spectral Classification of Embedded Stars (Berlin, Heidelberg: Springer Berlin Heidelberg), 1549–1553

André, P., Ward-Thompson, D., & Barsony, M. 1993, ApJ, 406, 122

Balick, B. & Brown, R. L. 1974, ApJ, 194

Bergman, P., Parise, B., Liseau, R., & Larsson, B. 2011, A&A, 527

Bergner, J. B., Martin-Domenech, R., Öberg, K. I., et al. 2019, ACS Earth Space Chem, 3, 8, 1564–1575

Bisschop, S. E., Jørgensen, J. K., Dishoeck, E. F. V., & Wachter, E. B. M. D. 2007, A&A, 465(3), 913–929

Bottinelli, S., Ceccarelli, C., B., L., et al. 2004, ApJ, 615, 354–358

Bottinelli, S., Ceccarelli, C., Williams, J. P., & B., L. 2007, A&A, 463, 601–610

Brown, R. D., Crofts, J. G., Godfrey, P. D., et al. 1975, ApJ, 197

Burke, D. J., Puletti, F., Brown, W. A., et al. 2014, MNRAS, 447(2), 1444–1451

Cazaux, S., M., T. A. G. G., C., C., et al. 2003, ApJ, 593

Ceccarelli, C. 2004, ASP Conference Series, 323

Ceccarelli, C., P., C., E., H., M., T. A. G. G., & E., C. 2006

Choi, M. 2009, ApJ, 705, 1730–1734

Clark, I. D. 1998, Isotope fractionation (Dordrecht: Springer Netherlands), 7354–357

Codella, C., Ceccarelli, C., Cabrit, S., et al. 2016, A&A, 586, L3

Codella, C., Ceccarelli, C., Caselli, P., et al. 2017, A&A, 605

Condon, J. J. & Ransom, S. M. 2018, Essential Radio Astronomy, https://www.cv.nrao.edu/~sransom/web/xxx.html, accessed: 15.09.2020

Crovisier, J., Bockele-Morvan, D., Biver, N., Colom, P., D. D., & Lis, D. C. 2004, A&A, 418, L35

De Simone, M., Ceccarelli, C., Codella, C., et al. 2020, ApJ, 896, L3

De Simone, M., Codella, C., Testi, L., et al. 2017, A&A, 99, A121

Dionatos, O., Jørgensen, J. K., Teixeira, P. S., Güdel, M., & Bergin, E. 2014, A&A, 563

Drozdovskaya, M. N., van Dishoeck E. F., M., R., Jørgensen, J. K., & K., A. 2019, MNRAS, 490, 50–79

Dunham, M. M.and Allen, L. E., Evans, N. J., I., Broekhoven-Fiene, H., et al. 2015, ApJS, 220, 11

Elsila, J. E., Glavin, D. P., & Dworkin, J. P. 2009, Meteorit Planet Sci, 44, 1323–1330

Favre, C., Bergin, E. A., Neill, J. L., et al. 2015, ApJ, 808:155

Gardner, F. F. & Winnewisser, G. 1975, ApJ, 195

Gargaud, M., Irvine, W., Amils, R., et al. 2015, Encyclopedia of Astrobiology, 595–596, 610–611, 861–864

Garrod, R. T. 2013, ApJ, 765(1)

Garrod, R. T. & Herbst, E. 2006, A&A, 457(3), 927–936

Gelder, M. L., Tabone, B., Tychoniec, L., et al. 2020, A&A, 639, A87

Goldsmith, P. F. & Langer, W. D. 1999, ApJ, 517, 209–225

Gudipati, M. S., Abou Mrad, N., Blum, J., et al. 2015, Space Sci. Rev., 197(1-4), 101–150

Herbst, E. & van Dishoeck, E. F. 2009, Annu. Rev. Astron. Astrophys., 47, 427

Hernández-Gómez, A., Sahnoun, E., Caux, E., et al. 2018, MNRAS, 483(2), 2014–2030

Hollis, J. M., Lovas, F. J., Jewell, P. R., & Coudert, L. H. 2002, ApJ, 571(1)

Hollis, J. M., Vogel, S. N., Snyder, L. E., Jewell, P. R., & Lovas, F. J. 2001, ApJ, 554(1)

Hull, C. L. H., Girart, J. M., Kristensen, L. E., Dunham, M. M., & et al. 2016, ApJ, 823

Hull, C. L. H., Girart, J. M., Tychoniec, L., & et al. 2017, ApJ, 847, 92

Hurt, L. & Barsony, M. 2009, ApJ, 460, L45

Imai, M., Sakai, N., Oya, Y., et al. 2016, ApJ, 830, L37

Jørgensen, J. K., Belloche, A., & Garrod, R. T. 2020, Annu. Rev. Astron. Astrophys., 58:1-55

Jørgensen, J. K., Bourke, T. L., Myers, P. C., et al. 2005, ApJ, 632, 973

Jørgensen, J. K., Müller, H. S. P., Calcutt, H., et al. 2018, A&A, 620

Jørgensen, J. K., Schöier, F. L., & van Dishoeck, E. F. 2002, A&A, 389, 908–930

Jørgensen, J. K., Wiel, M. H. D. V. D., Coutens, A., et al. 2016, A&A, 595

Krumholz, M. R. 2015, Notes on Star Formation

Kwok, S. 2012, Organic matter in the universe (Wiley-VCH)

Lada, C. J. 1987, IAU Symposium, 115, 1–18

Lamers, H. J. G. L. M. & Levesque, E. M. 2017, Understanding Stellar Evolution, 2514-3433 (IOP Publishing)

Lee, C., Codella, C., Li, Z., & Liu, S. 2019, ApJ, 876(1)

Loinard, L., Castets, A., Ceccarelli, C., et al. 2000, A&A, 359, 1169–1174

López-Sepulcre, A., Sakai, N., Neri, R., et al. 2017, A&A, 606, A121

Lykke, J. M., Coutens, A., Jørgensen, J. K., et al. 2017, A&A, 597

Manigand, S., Calcutt, H., Jørgensen, J. K., et al. 2019, A&A, 623

Manigand, S., Jørgensen, J. K., Calcutt, H., et al. 2020, A&A

Marcelino, N., Gerin, M., Cernicharo, J., et al. 2018, A&A, 620, A80

Martín-Doménech, R., Bergner, J. B., Öberg, K. I., & Jørgensen, J. K. 2019, ApJ, 880, 130

Mary, D., Theys, C., & Aime, C. 2013, New Concepts in Imaging: Optical and Statistical Models, Vol. 59, 157–187

Maury, A. J., Belloche, A., André, P., et al. 20014, A&A, 563, L2

Millar, T. J. 2005, A&G, 46

Mouschovias, T. C. 1976, ApJ, 206, 753–767

Myers, P. C. & Ladd, E. F. 1993, ApJ, 413

Öberg, K. I., Garrod, R. T., van Dishoeck, E. F., & Linnartz, H. 2009, A&A, 504, 891–913

Öberg, K. I., Lauck, T., & Graninger, D. 2014, ApJ, 788, 68

Occhiogrosso, A., Vasyunin, A., Herbst, E., et al. 2014, A&A, 564

Ospina-Zamudio, J., Lefloch, B., Ceccarelli, C., et al. 2018, A&A, 618, A145

Oya, Y., Sakai, N., Watanabe, Y., et al. 2017, ApJ, 837, 174

Partridge, A. A. & Wilson, R. B. 1965, ApJ, 142, 419–421

Persson, M. V., Jørgensen, J. K., Müller, H. S. P., et al. 2018, A&A, 610

Rohlfs, K. & Hüttemeister, S. 2009, Tools of Radio Astronomy, 5th edn. (Springer)

Rohlfs, K. & Wilson, T. L. 1999, Tools of Radio Astronomy (Springer)

Sahu, D., Liu, S.-Y., Su, Y.-N., et al. 2019, ApJ, 872, 196

Snyder, L. E. & Buhl, D. 1972, ApJ, 177, 619

Spezzano, S., S.Brünken, Schilke, P., et al. 2013, ApJL, 769:L19

Thaddeus, P., Vrtilek, J. M., & Gottlieb, C. A. 1985, ApJ, 299

Turner, B. E., Liszt, H. S., Kaifu, N., & Kisliakov, A. G. 1975, ApJ, 201

Vastel, C., Ceccarelli, C., Lefloch, B., & Bachiller, R. 2014, ApJ, 795

Yang, Y.-L., Evans, N. J., Smith, A., et al. 2020, ApJ, 891, 61

Zuckerman, B., Buhl, D., Palmer, P., & Snyder, L. E. 1970, ApJ, 160, 485